
11-17-2007

Modeling T Tauri Winds from He I λ 10830 Profiles

John Kwan

University of Massachusetts Amherst

Suzan Edwards

Smith College, sedwards@smith.edu

William Fischer

University of Massachusetts Amherst

Follow this and additional works at: https://scholarworks.smith.edu/ast_facpubs



Part of the [Astrophysics and Astronomy Commons](#)

Recommended Citation

Kwan, John; Edwards, Suzan; and Fischer, William, "Modeling T Tauri Winds from He I λ 10830 Profiles" (2007). Astronomy: Faculty Publications, Smith College, Northampton, MA.
https://scholarworks.smith.edu/ast_facpubs/19

This Article has been accepted for inclusion in Astronomy: Faculty Publications by an authorized administrator of Smith ScholarWorks. For more information, please contact scholarworks@smith.edu

MODELING T TAURI WINDS FROM He I λ 10830 PROFILES

JOHN KWAN,¹ SUZAN EDWARDS,² AND WILLIAM FISCHER¹

Received 2006 August 12; accepted 2006 November 17

ABSTRACT

The high opacity of He I λ 10830 makes it an exceptionally sensitive probe of the inner wind geometry of accreting T Tauri stars. In this line, blueshifted absorption below the continuum results from simple scattering of stellar photons, a situation that is readily modeled without definite knowledge of the physical conditions and recourse to multilevel radiative transfer. We present theoretical line profiles for scattering in two possible wind geometries, a disk wind and a wind emerging radially from the star, and compare them to observed He I λ 10830 profiles from a survey of classical T Tauri stars. The comparison indicates that subcontinuum blueshifted absorption is characteristic of disk winds in $\sim 30\%$ of the stars and of stellar winds in $\sim 40\%$. We further conclude that for many stars the emission profile of helium likely arises in stellar winds, increasing the fraction of accreting stars inferred to have accretion-powered stellar winds to $\sim 60\%$. Stars with the highest disk accretion rates are more likely to have stellar wind than disk wind signatures and less likely to have redshifted absorption from magnetospheric funnel flows. This suggests the possibility that when accretion rates are high, disks can extend closer to the star, magnetospheric accretion zones can be reduced in size, and conditions can arise that favor radially outflowing stellar winds.

Subject headings: planetary systems — stars: formation — stars: pre-main-sequence — stars: winds, outflows

1. INTRODUCTION

Young stars with accretion disks possess extended collimated mass outflows on spatial scales as small as a few AU (Hartigan et al. 2004; Dougados et al. 2000) to as large as a few parsecs (Bally et al. 2007). These ubiquitous outflows are almost certainly accretion powered, since there is a robust correlation between mass accretion and outflow rates over many orders of magnitude (Hartigan et al. 1995; Richer et al. 2000). The flows are thought to be launched via magnetohydrodynamic processes, where a large-scale open magnetic field is anchored to a rotating object, but whether that object is the disk or star or both is still uncertain (Ferriera et al. 2006). Disk winds may either emanate over a wide range of disk radii (Königl & Pudritz 2000) or be restricted to a narrow (X) region near the disk truncation radius (Shu et al. 1994), while stellar winds follow open field lines emerging radially from the star (Hartmann et al. 1982; von Rekowski & Brandenburg 2006; Romanova et al. 2005). Disk winds will aid in angular momentum transport in the disk and carry angular momentum away from the system (Pudritz et al. 2007), thereby affecting the evolution of the disk and any planets that may form there. Stellar winds in accreting systems are often regarded as of secondary importance, but recent work by Matt & Pudritz (2005) suggests otherwise. After raising serious questions as to whether a magnetic interaction between the disk and the star can provide the necessary spin-down for accreting stars, they posit that it is accretion-powered stellar winds that counteract the spin-up torque acquired by a star during disk accretion (Hartmann & Stauffer 1989) and are thus the primary agent for regulating stellar angular momentum in forming stars.

Observational constraints on the wind launch region are thus crucial for clarifying outflow origins and providing insight into the evolution of angular momentum in accretion disks and accreting stars, yet direct empirical tracers have been surprisingly

elusive. No evidence for winds is seen in molecular lines of CO and H₂O that arise in the inner accretion disk at radii from 0.1 to 2 AU. Rather, these lines show disk profiles that include turbulent broadening and warm disk chromospheres (Najita et al. 2003; Carr et al. 2004), and their symmetry belies no trace of outflowing gas from the upper disk layers. In contrast, atomic lines that form within 0.1 AU of the star, in particular, H α , Na D, Ca II H and K, and Mg II h and k (Appenzeller & Mundt 1989; Najita et al. 2000; Ardila et al. 2002), show clear evidence for inner winds at velocities of several hundred km s⁻¹ in many classical T Tauri stars (CTTSs) in the form of blueshifted absorption features superposed on broad emission. However, their utility as a wind diagnostic is limited, since the dominant contributor to the profile is the strong, broad, and centrally peaked emission that is generally interpreted as arising in magnetospheric infall zones (Muzerolle et al. 2001).

Recently, a new and quite robust diagnostic of the inner wind in accreting stars has been recognized. In contrast to the hydrogen lines, He I λ 10830 profiles in CTTSs and Class I sources show P Cygni–like profiles with deep blueshifted absorption below the continuum (Edwards et al. 2003; Dupree et al. 2005), reminiscent of those in stellar wind models developed to account for CTTS Balmer lines over a decade ago (Hartmann et al. 1990). It was in fact the inability of wind models to account for the structure of CTTS Balmer lines that led to the reinterpretation of these lines as arising in magnetospheric infall zones, which met with greater success in describing hydrogen emission profiles (Hartmann et al. 1994; Edwards et al. 1994). The extraordinary potential for He I λ 10830 to diagnose inner winds is revealed in a recent survey of classical T Tauri stars for which profiles show subcontinuum blueshifted absorption in $\sim 70\%$ of the stars, in striking contrast to H α , where only $\sim 10\%$ of CTTSs have blue absorption penetrating the continuum (Edwards et al. 2006, hereafter EFHK). The breadth and penetration depth of this subcontinuum blue absorption make He I λ 10830 an unprecedented probe of the wind geometry and acceleration region, providing for the first time the potential for good constraints on the launching region of the high-velocity inner wind.

¹ Five College Astronomy, University of Massachusetts, Amherst, MA; kwan@astro.umass.edu, wfischer@astro.umass.edu.

² Five College Astronomy, Smith College, Northampton, MA; sedwards@smith.edu.

In this paper, we look more deeply into the conclusion put forward in EFHK, that the diversity in the morphology of the subcontinuum blueshifted absorption at He I $\lambda 10830$ requires a range of inner wind geometries in accreting stars. Many CTTSs have P Cygni-like profiles, suggesting stellar winds, while others have narrow blue absorptions, suggesting disk winds. EFHK also find that both kinds of winds are likely accretion powered, as no evidence for winds is seen at $\lambda 10830$ in nonaccreting weak T Tauri stars (WTTSs), while among accreting CTTSs the combined strength of helium emission plus absorption is well correlated with the level of simultaneously measured $1 \mu\text{m}$ veiling, r_Y , defined as the ratio of continuum excess to the photospheric flux. The existence of helium-emitting winds in CTTSs was first suggested in a study of optical He I $\lambda 5876$ profiles (Beristain et al. 2001, hereafter BEK), which, in contrast to He I $\lambda 10830$, show several emission components, but no subcontinuum blueshifted absorption. Although these two helium transitions are intimately connected—the $\lambda 5876$ transition lies immediately before $\lambda 10830$ in a recombination/cascade sequence—the difference in their line profiles arises from the metastability of the lower level of He I $\lambda 10830$. While $\lambda 10830$ is optically thick, the absence of blue absorption at $\lambda 5876$ indicates that it traces the wind with optically thin emission. The contrast in optical depth for this pair of closely coupled lines thus offers a particularly potent means of diagnosing T Tauri winds.

Here we examine the origin of He I $\lambda 10830$ profiles in accreting stars by calculating theoretical profiles produced individually by both disk and stellar winds and comparing them to those from the EFHK survey. The frequent presence of absorption features in this line is due to its high opacity, because of the nature of the $2p^3P^o-2s^3S$ transition. The metastable lower level ($2s^3S$), 21 eV above the singlet ground state, will be significantly populated relative to other excited levels because of its weak de-excitation rate via collisions to singlet states. Since its upper level ($2p^3P^o$) has only $\lambda 10830$ as a permitted transition, absorption of a stellar continuum photon by this state will lead to reemission of a $\lambda 10830$ photon, unless the electron density is sufficiently high that collisional de-excitation ensues. We do not consider the latter regime here, and we model the $\lambda 10830$ line from the resonant scattering of continuum photons. The resulting line profile depends on the line opacity, but is insensitive to its value once it exceeds unity, so an examination of how the profile morphology depends on the geometric structure of the gas flow can be obtained quite readily by considering the case in which the gas flow is opaque to the stellar continuum at each velocity. These theoretical profiles for disk and stellar winds are presented for cases of pure scattering and scattering plus in situ emission in § 2. Their characteristics are summarized and compared with observed profiles, including both He I $\lambda 10830$ and He I $\lambda 5876$, in § 3. The discussion in § 4 addresses the relation between winds and accretion flows and the likely simultaneous presence of disk and stellar winds. A conclusion of our findings is given in § 5.

2. THEORETICAL LINE PROFILES

We present theoretical line profiles for two possible wind geometries, a disk wind and a wind emerging radially from the star. Both models predict profile morphologies (1) for pure scattering of stellar photons by the wind (absorption and subsequent reradiation) and (2) for scattering plus an additional source of in situ emission in the wind. A full Monte Carlo approach is followed only for the stellar wind, since, as explained in the following sections, the effects of secondary scattering on the emergent profile will be minor for the disk wind, but significant for the stellar wind. Geometric effects explored for stellar winds are disk shadowing, restricting

the wind to emerge from stellar polar regions, and restricting the origin of incoming photons to an axisymmetric ring on the stellar surface, as might be expected for radiation from a hot magnetospheric accretion shock. The resultant profile morphologies are compared with observed He I $\lambda 10830$ profiles for classical T Tauri stars in § 3.

2.1. Disk Wind Line Profiles

An azimuthally symmetric disk wind is assumed to flow away from the disk along streamlines tilted at an angle θ_w from the normal to the disk plane. This wind opening angle is always $\theta_w > 30^\circ$, as required for magnetocentrifugal launching (Blandford & Payne 1982). The wind is launched between an inner radius ρ_i , at which the disk is truncated, and an outer radius ρ_f , where ρ is the distance along the disk plane from the star measured in units of R_* , the stellar radius. It is reasonable to expect the terminal poloidal velocity of the gas launched from ρ to scale with the escape velocity, which is $\propto \rho^{-1/2}$, and the distance to reach this terminal value to scale with ρ . We thus assume a simple poloidal velocity law that encompasses these relations with $v_p = 540\rho^{-1/2}(1 - \rho/r)^{1/2} \text{ km s}^{-1}$, where r is the radial distance from the star, also in units of R_* , and the scaling factor establishes the maximum terminal velocity (for $\rho_i = 2$) as 382 km s^{-1} , in line with observed values. The exact details of the gas acceleration are not crucial, so long as the poloidal velocity increases monotonically from zero to the terminal value, because we also assume the disk wind to be opaque in the scattering transition (representing He I $\lambda 10830$) at each position. This assumption on the opacity ensures, for an optimal comparison with the stellar wind models, the maximum breadth and depth of the continuum absorption that can be produced by a disk wind scattering stellar photons. If the line becomes optically thin at some distance away from the disk plane, which is possible and likely, the resultant absorption from a disk wind will be weaker, particularly at the high-velocity end, than the model one.

The angular velocity of the disk where each streamline is anchored is specified by $\Omega = (300 \text{ km s}^{-1}/R_*)\rho^{-3/2}$. We examine the effects of rotation in the disk wind for two extreme cases. In one case, each individual streamline rotates at a rate that conserves angular momentum. In the other case, each streamline rotates rigidly. These two extremes should encompass the realistic case of rigid rotation close to the disk and rotation with conservation of angular momentum farther away.

With the assumption of a completely opaque scattering transition, the absorption component of the profile simply reflects the contour area projected by the disk wind against the star at each line-of-sight velocity. An absorbed stellar photon is assumed to be reemitted isotropically, and right away it either escapes to infinity or hits the star or disk. In contrast to the stellar wind simulations in § 2.2, we have not followed the detailed photon path of multiple scatterings, since in this case the scattered photons will not appreciably alter the morphology of the narrow absorption component. This is because in a disk wind more photons are scattered out of a viewing angle intersecting the wind than into the same viewing angle, and those that are scattered into the same viewing angle are very much broadened by the large bulk velocity (rotational and poloidal motions) of the flow, so they are widely distributed in velocity.

Predicted line profiles from disk winds are shown in Figures 1 and 2, with model parameters listed in Table 1. The first figure is for pure scattering, and the second figure includes additional contributions from in situ emission (see below). In both figures the wind opening angle is $\theta_w = 45^\circ$, and $\rho_i = 2$. In Figure 1 cases are shown for both $\rho_f = 4$ and 6, but only for $\rho_f = 4$ in Figure 2.

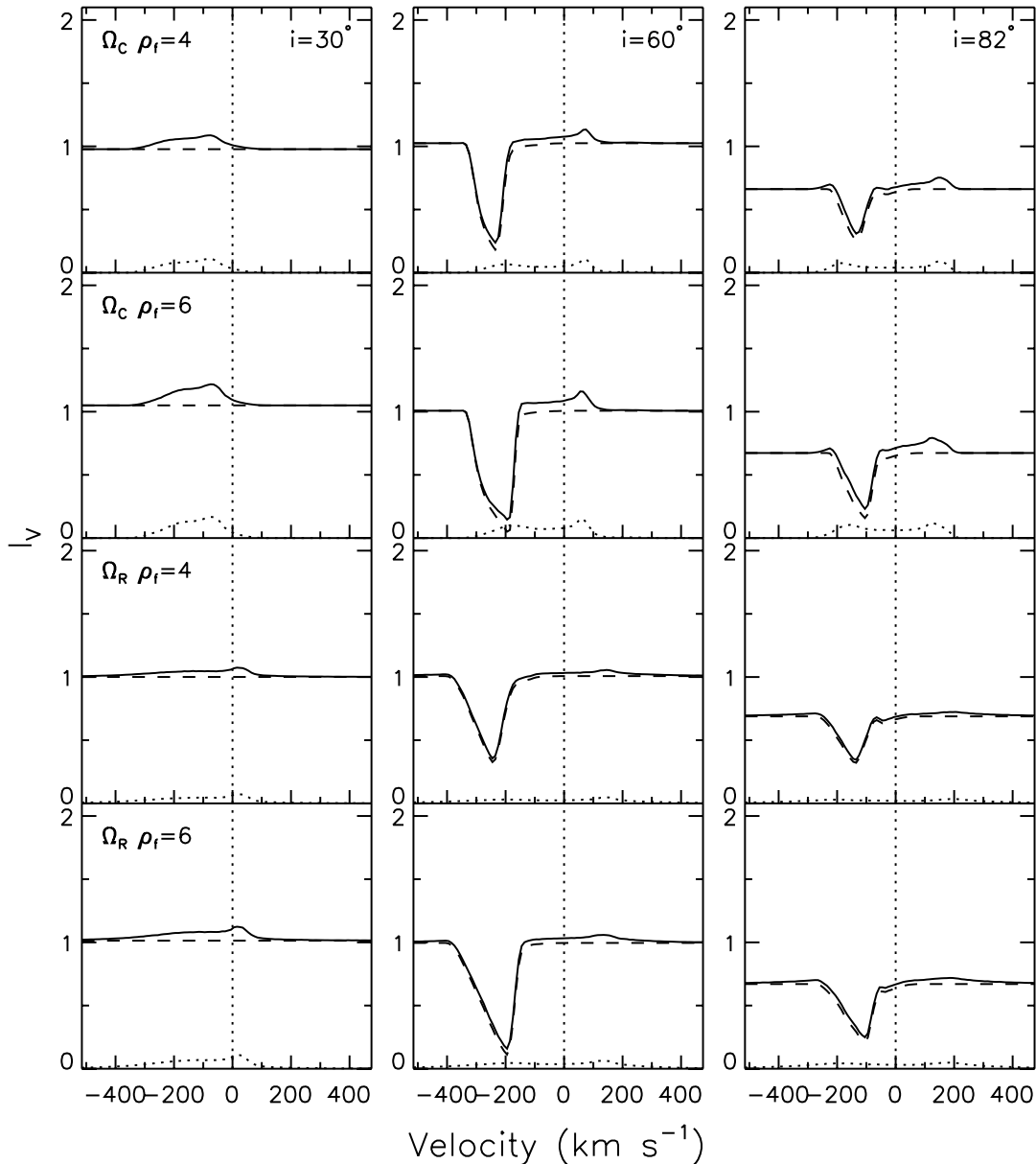


FIG. 1.— Disk wind: theoretical line profiles produced from scattering of the stellar continuum by a disk wind emanating at 45° from the disk normal. Within each panel, the dashed line shows the profile of the absorbed stellar continuum, the dotted line shows the profile of the scattered photons, and the solid line shows the summed emergent profile. The three columns denote, from left to right, viewing angles $i = 30^\circ$, 60° , and 82° . The top two rows illustrate the case in which the disk wind rotates with conservation of angular momentum, Ω_C , and the bottom two rows illustrate the case of rigid rotation, Ω_R . In each rotation case, the upper row has the disk wind originating from 2 to $4 R_*$, and the lower row from 2 to $6 R_*$.

Columns show three viewing angles, $i = 30^\circ$, 60° , and 82° . The top two rows show the case of conservation of angular momentum (Ω_C), and the bottom two rows show the case of rigid rotation (Ω_R). The solid line shows the resultant profile, which is a sum of the absorption of the continuum (*dashed line*), the emission from scattered photons (*dotted line*), and in situ emission (*shaded area*), if present. Slight deviations from unity in the continuum level at $i = 30^\circ$ and 60° are statistical fluctuations caused by the finite number of photons used in the simulation. The much lower continuum level at $i = 82^\circ$ is due to disk occultation.

For the pure scattering case in Figure 1, at viewing angles less than the opening angle of the wind, $i < 45^\circ$, the resultant profiles are purely in emission and almost entirely blueshifted, because of disk occultation of the receding wind. They are also quite broad ($>300 \text{ km s}^{-1}$), more so for the case of rigid rotation, because of the larger rotational broadening. For viewing angles exceeding

the opening angle of the wind, $i > 45^\circ$, the line of sight to the star crosses the wind streamlines, and the profile is prominently in absorption. The emission contributed from the scattered photons is weak compared to the absorption, because there is no scattering into $i > \theta_w$ from continuum absorption at $i < \theta_w$ and because of disk occultation.

The distinctive aspect of absorption features from a disk wind is that they are narrow in comparison to the full range of velocities in the accelerating wind, never extending over the whole possible range from rest to terminal velocity, despite the assumption of high opacity. This is because at a particular viewing angle most lines of sight toward the star will intercept only a small portion of the full range of wind velocities; those toward the stellar polar region intersect the wind near its terminal speed, while those toward the stellar equatorial region intersect the wind at low velocities. Thus, in the summed emergent profile only a

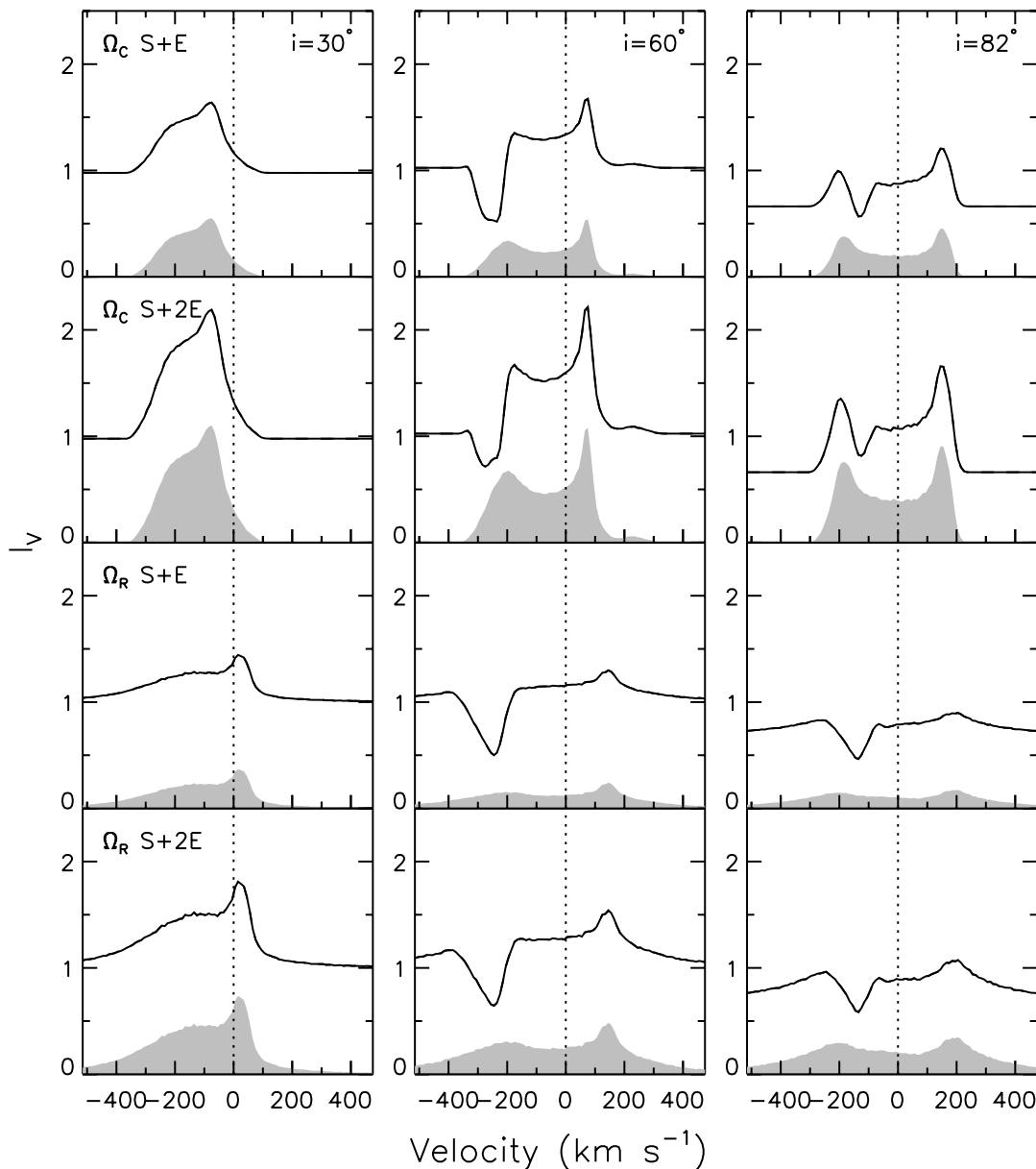


FIG. 2.—Disk wind: theoretical line profiles from a disk wind emanating at $\theta_w = 45^\circ$ with in situ emission added to pure scattering. Shaded areas show the in situ contribution, scaled at 5 times the scattered emission (5S) in rows 1 and 3 and 10 times the scattered emission (10S) in rows 2 and 4, and the solid line is the emergent profile. As in Fig. 1, columns reflect viewing angles from $i = 30^\circ$ to 82° ; the top 2 rows show rotation with conservation of angular momentum Ω_C , and the bottom two rows show rigid rotation, Ω_R . All cases have $\rho_i = 2$ and $\rho_f = 4$.

TABLE 1
GUIDE TO FIGURES FOR DISK WIND MODELS (SINGLE SCATTERING)

Figure (1)	θ_w (deg) (2)	ρ_i (3)	ρ_f (4)	Rotation (5)	Emission (6)	i (deg) (7)
1.....	45	$2R_*$	$4R_*, 6R_*$	Ω_C, Ω_R	S	30, 60, 82
2.....	45	$2R_*$	$4R_*$	Ω_C, Ω_R	S + E, S + 2E	30, 60, 82

NOTES.—Col. (2): wind opening angle, measured from disk normal; col. (3)–(4): range of disk radii for wind launching; col. (5): angular momentum conservation Ω_C , rigid rotation Ω_R ; col. (6): emission component is either pure scattering (S) or pure scattering plus in situ emission (E), where $E = 5S$ has a magnitude comparable to the wind absorption; col. (7): viewing angle, measured from disk normal.

small range of projected velocities will be encountered by lines of sight sufficient to produce a significant absorption. Similar reasoning also accounts for a shift in the centroid of the absorption feature toward a smaller blueshift as i increases and the earlier part of the acceleration region is preferentially intercepted. The absorption does not bottom out, because at no observed velocity is the stellar continuum completely covered.

In addition to their dependence on viewing angle, the width and centroid of the absorption component will also be affected by the range of radii in the disk over which the wind is launched. For our inner launch radius of $\rho_i = 2$, we explore outer launch radii from $\rho_f = 4$ to $\rho_f = 6$. Although these maximum launch radii are smaller than the full range expected for an extended disk wind, this choice is appropriate for the region of helium excitation, which will be restricted to the inner disk, which is also where the high-speed components of jets arise. It can be seen by comparing the first row ($\rho_f = 4$) with the second row ($\rho_f = 6$) for each

rotation case in Figure 1 that the blue absorption extends toward lower velocities when ρ_f is increased and more streamlines of comparatively lower velocities are seen through. The effect of changing ρ_i can be seen from difference profiles between the first and second rows, where a narrower width and less blue centroid would arise from a wind launched between $\rho_i = 4$ and $\rho_f = 6$. In addition, the line width will be affected by rotation, as shown for the two extreme cases we have examined, where the absorption has a slightly larger width when the disk wind rotates rigidly (Ω_R).

Changing θ_w will not appreciably alter the profile characteristics. A wider opening angle at the same i shifts the centroid of the absorption blueward and makes it slightly broader. This results because the streamline is then more closely aligned with the viewing angle and because the gas speed is higher at the intersection point (a larger value of r/ρ in the expression for v_p). Wider opening angles also reduce the probability of observing an absorption profile, which requires $i > \theta_w$. Narrower opening angles will reverse these effects, but must always be $\theta_w > 30^\circ$.

The effect of including a contribution from in situ emission in the disk wind is shown in Figure 2. We simply assume that the in situ emission line profile has a kinematic structure identical to the profile of scattered photons, since its main characteristics come from the large bulk velocity at each point of the wind from the combined rotational and poloidal motions, and the line profile will depend only weakly on the excitation details. To illustrate its effect on the profile, we adopt a value for the in situ contribution that is comparable to the magnitude of the absorption. In this case the in situ emission is 5 times the scattered emission ($E = 5S$). We also include a case where it is twice as strong as the absorption ($E = 10S$). As in Figure 1, the first 2 rows of Figure 2 are for the case of conservation of angular momentum, and the last two are for rigid rotation, where now the first row in each case is the smaller, and the second the larger, contribution from in situ emission. It is seen that the effect of this additional source of emission does not significantly alter the profile morphology. Although the broad, flat emission is more prominent than before, the sharp blue dip will still be visible, because the large bulk motions distribute the emission broadly over all velocities. At viewing angles inside the wind opening angle, where no absorption is formed, the broad, blue-shifted emission is now quite prominent. As the viewing angle increases, the blue absorption becomes apparent, still narrow compared with the extent of the emission and decreasing in velocity as the viewing angle increases. At the same time, the emission shifts to a more centered, but very broad profile, clearly showing the distinctive double-horned structure characteristic of rotation.

The above profile characteristics of disk winds are inherent to the location of the wind relative to the star and the geometry of the streamline, with a strong aspect dependence, which is influenced by whether the viewing angle is interior or exterior to the wind opening angle. Our assumption of a completely opaque scattering transition ensures that the model profiles show the maximum possible blueshifted absorption from a disk wind. In § 2.2, we examine the case of a stellar wind in which the geometry of the acceleration process, radially away from the center of the star, enables each line of sight toward the center of the star to see through the full velocity range from 0 to the terminal value.

2.2. Stellar Wind Line Profiles

We first examine the simple case of a spherical, radial stellar wind originating from an inner radius r_i and having a velocity law given by $v = v_t(1 - r_i/r)^{1/2}$, where v_t is the terminal velocity.

This velocity law is analogous to the one used for the disk wind, except that there is only one origination radius. Our models also allow for the presence of a geometrically flat disk, with a truncation radius specified by ρ_T .

The stellar wind calculation differs from that of the disk wind in several ways. First, we relax the assumption of a completely opaque transition, and second, we employ a Monte Carlo, rather than single scattering, simulation of the radiative transfer. The first change is made to accommodate the observed profiles in the EFHK survey with a P Cygni-like character that show blue absorptions tapering toward the continuum at the highest velocities, indicating that the line is becoming optically thin. We assume a simple radial dependence for the density in the lower state of the scattering transition representing He I λ 10830; i.e., $n_{2^3S} \propto (r_i/r)^\alpha v_l/(v + v_l)$, where α is a parameter and v_l , taken to be 30 km s^{-1} , avoids divergence at $v = 0$. The line opacity as a function of velocity is determined by a suitable choice of α , so that the line opacity ranges from being much greater than 1 at low velocities, thereby producing a troughlike absorption, to less than 1 at high velocities, thereby producing a tapering toward the continuum. The outflow is also given a turbulence velocity width $\Delta v_{\text{tb}} = \Delta v_i(r_i/r)^\beta$, with parameters Δv_i and β . Two cases are considered, a low-turbulence one (T_L : $\Delta v_i = 10 \text{ km s}^{-1}$ and $\beta = 0$) and a high-turbulence one (T_H : $\Delta v_i = 100 \text{ km s}^{-1}$ and $\beta = 2$). The extreme value for the high turbulence is chosen because one observed CTTS profile (DR Tau) shows a broad blue absorption extending redward of the stellar velocity by up to 100 km s^{-1} . For the low- and high-turbulence cases, α is taken to be 6 and 5, respectively.

The adoption of a full Monte Carlo approach is necessary here because, in contrast to the disk wind case, the absorption of the stellar continuum by a stellar wind will be substantially filled in by scattered photons. This requires that we obtain the profiles with a Monte Carlo simulation so the full path can be traced for each photon until it either escapes to infinity or hits the star or the disk.

As in the disk wind, we examine the effects of allowing the wind gas to produce in situ emission in addition to scattering of the stellar continuum, representing the possibility of the additional production of He I λ 10830 photons via recombination/cascade and/or collisional excitation. In this case, however, the in situ emission profile is derived from a Monte Carlo simulation, parameterized with a rate $\propto n_{2^3S}(r_i/r)^\gamma$. The effect of changing γ from 0 to 2, corresponding to successively smaller contributions from the outer, higher speed gas, has a small effect on the emitted profiles, and the ones shown are for $\gamma = 1$. As for the disk wind simulation, we choose the magnitude of the in situ emission (E) to be comparable to the absorption strength of the stellar continuum, so that the summed line profile ($S + E$) will illustrate an intermediate case between pure scattering and dominant in situ emission.

Figures 3, 4, and 5 illustrate profiles for a spherical stellar wind originating at $r_i = 1.5R_*$, with 3 different disk truncation radii and four different sets of wind assumptions, as summarized in Table 2. This set of models shows clearly the effect of disk shadowing, which depends on the relative sizes of the wind origination and disk truncation radii. There will be no shadowing effect when the disk truncation radius is large compared to the wind origination radius, $\rho_T > 5r_i$, while the effect will be significant when $\rho_T \leq r_i$. Thus, the ratio ρ_T/r_i determines the disk-shadowing effect. Profiles for a particular ratio would be the same were it not for the additional effects of stellar occultation, which will be more important when r_i is closer to R_* .

Figure 3 shows a spherical wind with no disk. Although accretion disks are present in all the classical T Tauri stars whose

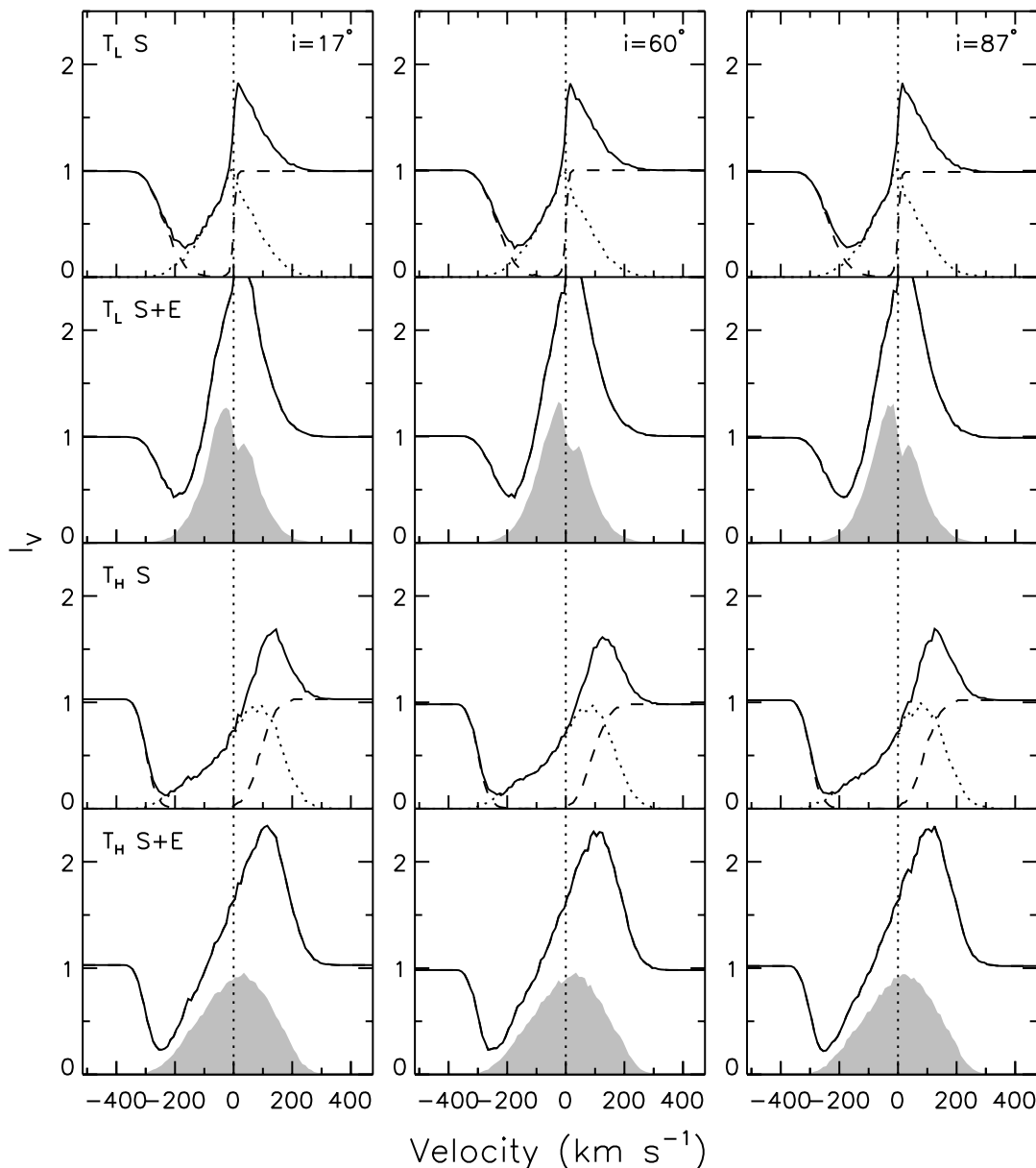


FIG. 3.— Stellar wind: theoretical profiles obtained by Monte Carlo simulation of line formation in a radially expanding spherical wind originating at $r_i = 1.5R_*$ in the absence of disk occultation ($\rho_T > 5r_i$). The top two rows represent the low-turbulence case, T_L , and the lower two rows represent the high-turbulence case, T_H . For each turbulence case, the first row is for pure scattering of the stellar continuum (S), and the second row includes additional in situ emission ($S + E$). The shaded regions show the in situ contribution, scaled to be comparable in strength to the scattering absorption. Although there is no viewing angle dependence in the absence of a disk, the figure is formatted for ready comparison with the remaining figures, and vertical columns denote three viewing angles, $i = 17^\circ$, 60° , and 87° , measured from the disk normal.

helium profiles we are modeling, this set of wind profiles would apply to those disks where disk shadowing is not important, i.e., where the inner truncation radius is large compared to the starting point for the wind, $\rho_T > 5r_i$. The case of extreme disk shadowing is shown in Figure 4 for a disk reaching to the stellar surface ($\rho_T = 1$). However, similar profiles would result as long as the wind origination radius much exceeds the disk truncation radius, $\rho_T \leq 0.5r_i$. Figure 5 illustrates an intermediate case, where the disk is truncated at a distance that is only 1.5 times the starting point for the wind, $\rho_T = 1.5r_i$. In each figure the three vertical columns represent views from more pole-on to more edge-on configurations, $i = 17^\circ$, 60° , and 87° . In the diskless case of Figure 3 we present profiles for the same three viewing angles to ensure similar proportions among all the figures and facilitate comparison of profile morphology with the cases including disk shadowing. As expected, in the absence of a disk there is no de-

pendence on i , although small effects from the finite statistics in the Monte Carlo simulation can be seen on close inspection.

The four horizontal rows in Figures 3, 4, and 5 correspond to four different assumptions about the stellar wind. In all four cases the wind originates at the same distance from the star, $r_i = 1.5$, and has the same terminal velocity, $v_t = 375 \text{ km s}^{-1}$, chosen to be comparable to the maximum terminal velocity in the disk wind. Two cases (top two horizontal rows) represent models with low turbulence (T_L) and the other two cases (bottom two horizontal rows) represent models with high turbulence (T_H) plus a somewhat higher optical thickness of the gas ($\alpha = 5$, rather than 6). For each turbulence case, the profiles in the upper row are formed simply from scattering of the $1 \mu\text{m}$ stellar continuum photons, where the dashed line shows the absorption of this continuum, the dotted line shows the profile of the photons scattered into the line of sight, and the dark solid line shows the summed

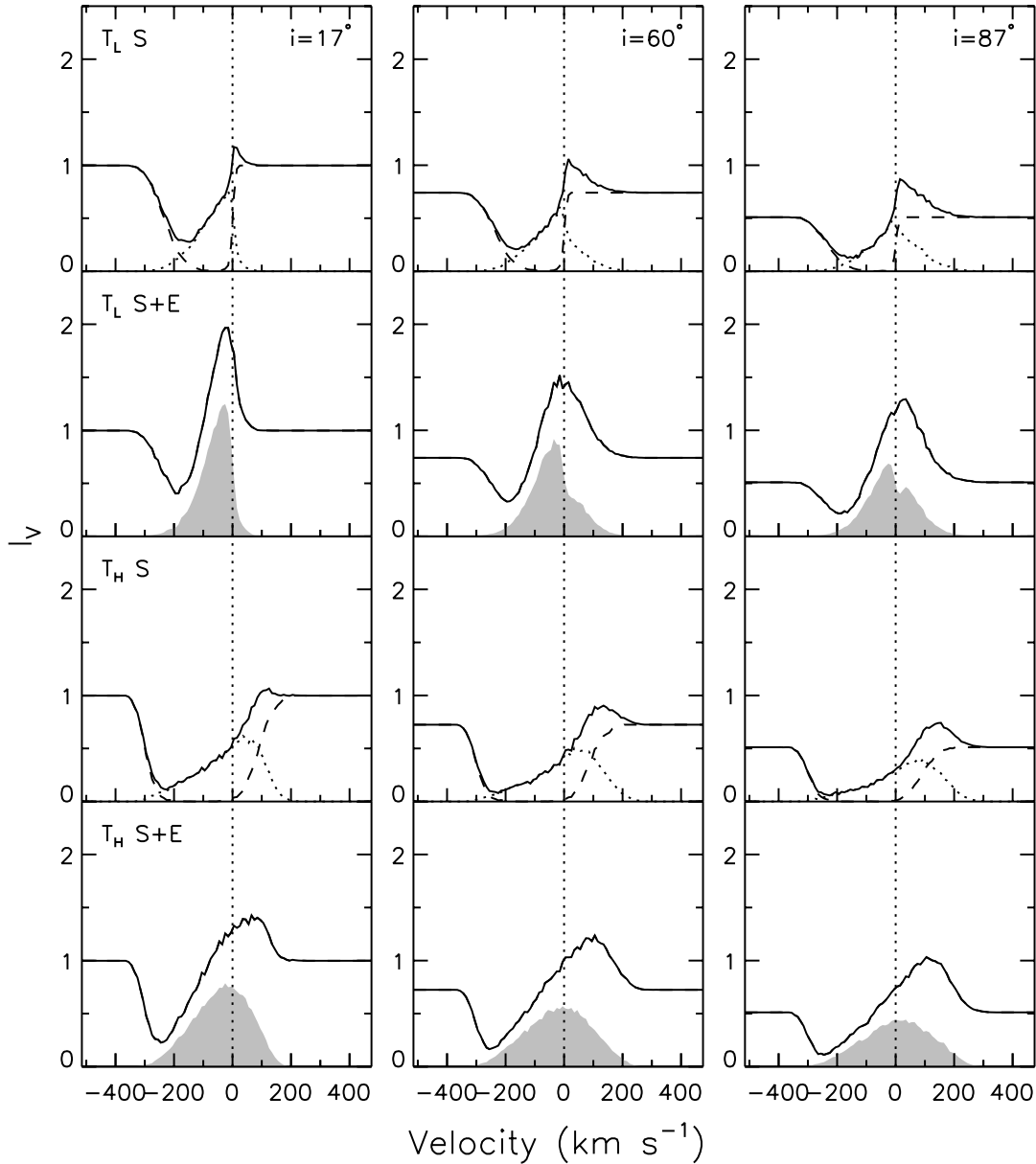


FIG. 4.—Stellar wind: same spherical wind as in Fig. 3, but now including the effects of disk shadowing (important when $\rho_T \leq r_i$). Here the disk reaches to the stellar surface, $\rho_T = 1R_*$ and $r_i = 1.5R_*$. For each turbulence case (T_L and T_H) profiles without and with in situ emission contributions (S and $S + E$) are shown. Vertical columns denote three viewing angles, $i = 17^\circ$, 60° , and 87° , measured from the disk normal.

emergent profile. The lower row of each turbulence case includes the effects of additional in situ emission in the wind, where the shaded region shows the contribution from in situ emission alone and the solid line is the emergent profile resulting from summing this with the pure scattering profile from the previous row.

The occultation effect of the disk on the line profiles is manifest in three ways. One, theoretically significant but difficult to establish observationally, is that the stellar continuum is dependent on viewing angle. In the $\rho_T = 1$ disk the continuum level drops steadily from 1 to 0.5 as i increases from pole-on (0°) to edge-on (90°), and in the $\rho_T = 1.5r_i$ disk it remains at 1 for $i < 64^\circ$ and then drops toward 0.5 at $i = 90^\circ$.

The other two effects directly impact the profile morphology, altering the *net* equivalent width and the centroid of the emission component. In the diskless case (Fig. 3) the intrinsic wind profile from pure scattering has a P Cygni character, with prominent

blue absorption and red emission components. Its net equivalent width is somewhat negative (i.e., absorption exceeds emission), rather than zero, because of stellar occultation, and this effect is more pronounced in the case of high turbulence (row 3), because of the preferential backscattering of the stellar photons. The presence of a disk has a minimal occultation effect on the line profile for edge-on views, but this becomes significant for more pole-on views. Although all three disk cases have similar pure scattering profiles after normalization of the continuum level at $i = 87^\circ$, as i decreases the net equivalent width for the $\rho_T = 1$ disk becomes more pronouncedly negative, and by $i = 17^\circ$ there is hardly any red emission, and the observed profile is entirely in absorption. In the $\rho_T = 1.5r_i$ disk the line profile at $i = 60^\circ$ is intermediate between those of the other two disks, while at $i = 17^\circ$ it becomes like that of the diskless case. This is because, given the acceleration law, the gas reaches $0.58v_i$ at $r = 1.5r_i$, so a large part of the photon absorption occurs within this radius, and the hole in the disk

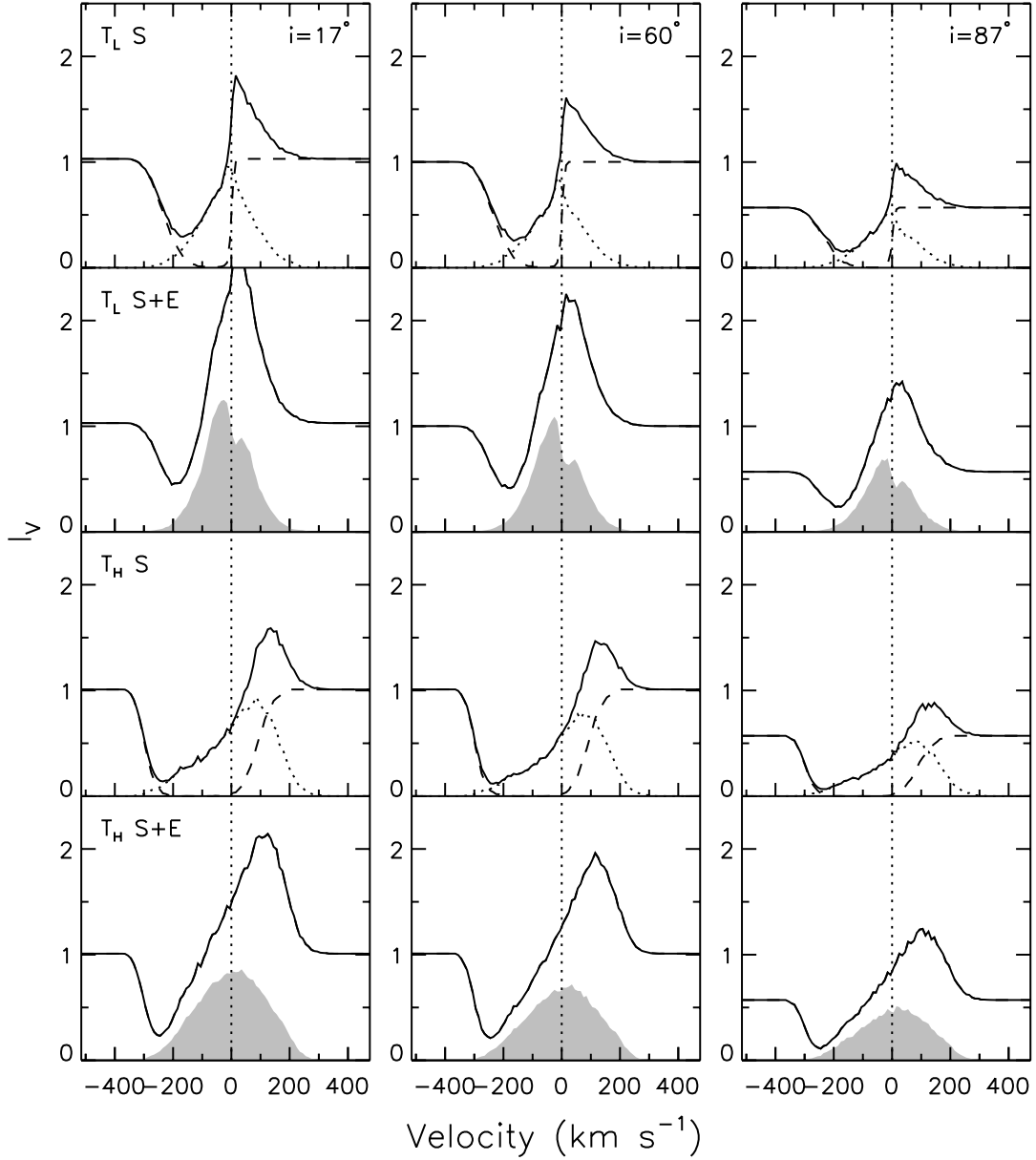


FIG. 5.— Stellar wind: same as Fig. 3, but in the presence of a disk truncated at $\rho_T = 2.25R_*$. For each turbulence case (T_L , and T_H), profiles without and with in situ emission contributions are shown (S and $S + E$). Vertical columns denote three viewing angles, $i = 17^\circ$, 60° , and 87° , measured from the disk normal.

TABLE 2
GUIDE TO FIGURES FOR STELLAR WIND MODELS (MONTE CARLO)

Figure (1)	r_i (2)	ρ_T (3)	Turbulence (4)	θ_w (deg) (5)	Continuum (6)	Emission (7)	i (deg) (8)
3.....	1.5	>7.5	T_L, T_H	90	Star	$S, S + E$	17, 60, 87
4.....	1.5	1.0	T_L, T_H	90	Star	$S, S + E$	17, 60, 87
5.....	1.5	2.25	T_L, T_H	90	Star	$S, S + E$	17, 60, 87
6.....	3.0	3.0	T_L, T_H	60	Star	$S, S + 2E$	17, 60, 87
7.....	3.0	3.0	T_L	60	Star	$S + 2E$	17–87
8.....	1.5	1.0	T_L	90	Rings	S	17, 60, 87

NOTES.— Col. (2): Inner wind radius in units of R_* ; col. (3): disk truncation radius in units of R_* ; col. (4): low turbulence T_L ($\Delta v_{\text{th}} = 10 \text{ km s}^{-1}$) or high turbulence T_H [$\Delta v_{\text{th}} = 100(r_i/r)^2 \text{ km s}^{-1}$]; col. (5): wind emergence angle from stellar pole (either spherically symmetric or polar); col. (6): continuum photons emerge either from the star or rings at 30° , 60° , 74° , or 82° from the stellar pole; col. (7) emission is either pure scattering (S) or includes in situ emission (E) scaled to be comparable to the wind absorption; col. (8) viewing angle, measured from disk normal.

allows most of the photons scattered by the receding stellar wind to come through at small inclination angles. Hence, a large negative net equivalent width requires the disk truncation radius ρ_T be comparable to or smaller than the wind origination radius r_i .

The second observable effect of disk occultation is altering the centroid of any in situ emission. This is most evident in the low-turbulence case (second row from top). In the $\rho_T = 1R_*$ disk (Fig. 4) at $i = 87^\circ$ the in situ emission profile (shaded area) is nearly symmetric about $v = 0$, the stellar velocity. (The slight depression in the in situ emission immediately to the red of $v = 0$ and the slightly weaker red side is caused by stellar occultation.) But, as i decreases and more of the receding stellar wind is occulted, the emission profile becomes progressively more blueshifted. This characteristic of a line purely in emission is often indicative of the presence of outflowing gas in the presence of an obscuring disk. When both scattering and in situ emission contributions are roughly comparable, the emergent profile also reveals a blueshifted emission centroid. Thus, the emergent profiles with in-situ emission show that, when disk shadowing is not important, the emission component of the observed profile has a red centroid, but the emission progresses from red to blue centroids as disk shadowing becomes more effective.

We included calculations with extreme turbulence because the DR Tau profile shows a broad blue absorption extending redward of the stellar velocity by up to 100 km s^{-1} . The high-turbulence case we considered (Fig. 4, row 3) does successfully reproduce this effect. It also leads to a preferential backscattering of the stellar photons, thereby producing a redshifted centroid in the profile of the scattered photons, which is clearly seen in the diskless case (Fig. 3, dotted line). In the $\rho_T = 1R_*$ disk (Fig. 4) it is most obvious at $i = 87^\circ$, but is still noticeable at $i = 17^\circ$, despite disk occultation of some of the red photons, in comparison with the low-turbulence case (row 1). The combination of these two effects of turbulence, namely, extending the blue absorption redward of the stellar velocity and creating a redshifted scattering profile, is a more distinct and well-displaced red emission centroid in the emergent profile for pure scattering. The backscattering is much more important for the stellar photons, which propagate into the wind along \hat{r} , than for the photons generated in the wind, which are emitted with an initial isotropic distribution in direction (compare the dotted line in row 3 with the shaded area in row 4). Instead, the effect of turbulence on the in situ emission components is to broaden them, while disk occultation makes them more blueshifted for more face-on orientations. The combined scattering plus emission profile then shows an emission centroid whose position is dependent on viewing angle. (Here the in situ emission profiles are shown with $\gamma = 1$; for $\gamma = 0$ and 2, the corresponding profile will be similar, but slightly broader and narrower, respectively.)

All of the previous stellar wind models assume the wind is spherically symmetric. However, a more likely scenario for an accretion-powered stellar wind is that it will emerge primarily from polar latitudes on the star, above regions where stellar magnetic field lines couple to the disk. To assess the effects of a restricted range of latitudes for the emergence of the wind in the presence of disk shadowing, we show in Figures 6 and 7 profiles for the case of a wind emerging only within 60° of the stellar poles. In this simulation the wind origination radius is expanded to $r_i = 3R_*$, and the disk truncation ρ_T is set equal to the wind origination radius r_i . The strength of the in situ emission in this case is double that in previous ones to compensate for the smaller volume in the polar wind.

As expected, in the pure scattering case for the polar wind model shown in Figure 6, the subcontinuum blue absorption in the emergent profile remains deep and broad at $i < 60^\circ$, becomes

half as strong at $i = 60^\circ$, rapidly diminishes as i increases further, and disappears at $i > 71^\circ$. When the blue absorption is prominent, the overall profile morphology is still P Cygni-like in the low-turbulence case. However, in the high-turbulence case, the profile is significantly modified at small viewing angles, where the red emission above the continuum is much less conspicuous. This results not from disk shadowing (pure scattering profiles calculated with $\rho_T = 1.5r_i = 4.5R_*$ are nearly the same), but from the absence of wind gas at $90^\circ \geq \theta > 60^\circ$. While at low viewing angles the absorption of the stellar continuum (e.g., at $i = 17^\circ$) remains the same as in the case of $\theta_w = 90^\circ$, the absence of wind gas at $90^\circ \geq \theta > 60^\circ$ contributes no scattered photons from that sector. This contribution would, at $i = 17^\circ$, be centered about $v = 100 \text{ km s}^{-1}$ (see Fig. 5 for $\theta_w = 90^\circ$, $r_i = 1.5$, and $\rho_T = 1.5r_i$). This effect is less dramatic in the low-turbulence case, where the emission part of the emergent profile, although weaker in comparison with the case of $\theta_w = 90^\circ$, is still conspicuous. This is because the contribution to photons scattered into $i = 17^\circ$ from absorption by the $90^\circ \geq \theta > 60^\circ$ sector now centers about $v = 0 \text{ km s}^{-1}$. Also, when the turbulence is weak, the velocity gradient is the dominant factor in radiative transfer, and the larger velocity gradient along \hat{r} or $-\hat{r}$ is higher than that along a direction normal to \hat{r} . So a photon absorbed in the $90^\circ \geq \theta > 60^\circ$ sector is less likely to be scattered into $i = 17^\circ$. These characteristics can also be deduced from the in situ emission profiles. Comparing the shapes (not magnitudes, because of the different normalization factors) of the shaded profiles at $i = 17^\circ$ between Figures 6 and 5 reveals the contribution from the $90^\circ \geq \theta > 60^\circ$ sector to the in situ emission profiles.

Additional profiles for the same polar wind model with low turbulence and in situ emission are shown in Figure 7, but with a finer grid of viewing angles to illustrate more clearly how the profile morphology changes with inclination. Looking at the in situ emission profile by itself first (shaded areas), it has a blue centroid except at $i = 87^\circ$. With $\rho_T = r_i$, the degree of blueshift is highest at $i \sim 60^\circ$ and decreases as i moves toward 0° or 90° . Clearly, as ρ_T decreases toward 1.0, the degree of blueshift increases more rapidly with more pole-on views. For the same ρ_T/r_i , the in situ emission profile for $\theta_w = 60^\circ$ is more blueshifted than the corresponding one for $\theta_w = 90^\circ$. When the in situ emission and the scattering of the stellar continuum are included together, the combined profile shows that the part above the continuum changes from having a red centroid to having a blue centroid. This figure clarifies how a polar wind generates a wide range of emergent profiles, including some with no blueshifted absorption, and illustrates how the presence of disk shadowing generates emission with blue centroids for most viewing angles.

We also explored one other situation for the stellar wind models, motivated by the fact that several CTTSs with stellar wind signatures in the He I λ 10830 profiles have $1 \mu\text{m}$ veilings exceeding 1.0. To assess whether scattering of photons from a continuum source that is localized to rings on the star is significantly different from scattering a continuum originating from the entire stellar surface, we have examined the case of photons originating solely from an isotropically radiating continuum located as an axisymmetric ring at polar angle θ_v of the star and of angular width about θ_v given by $\Delta \cos \theta = 0.1$. This simulation was carried out for a disk reaching to the stellar surface, $\rho_T = 1$, and the low-turbulence case. Figure 8 shows the resulting line profiles, ordered from top to bottom, for $\theta_v = 30^\circ, 60^\circ, 74^\circ$, and 82° , respectively. The $\theta_v = 60^\circ$ profiles are almost identical to the ones formed from scattering of a continuum emerging from over the whole star. The $\theta_v = 30^\circ$ profiles exhibit the most noticeable difference, primarily because the

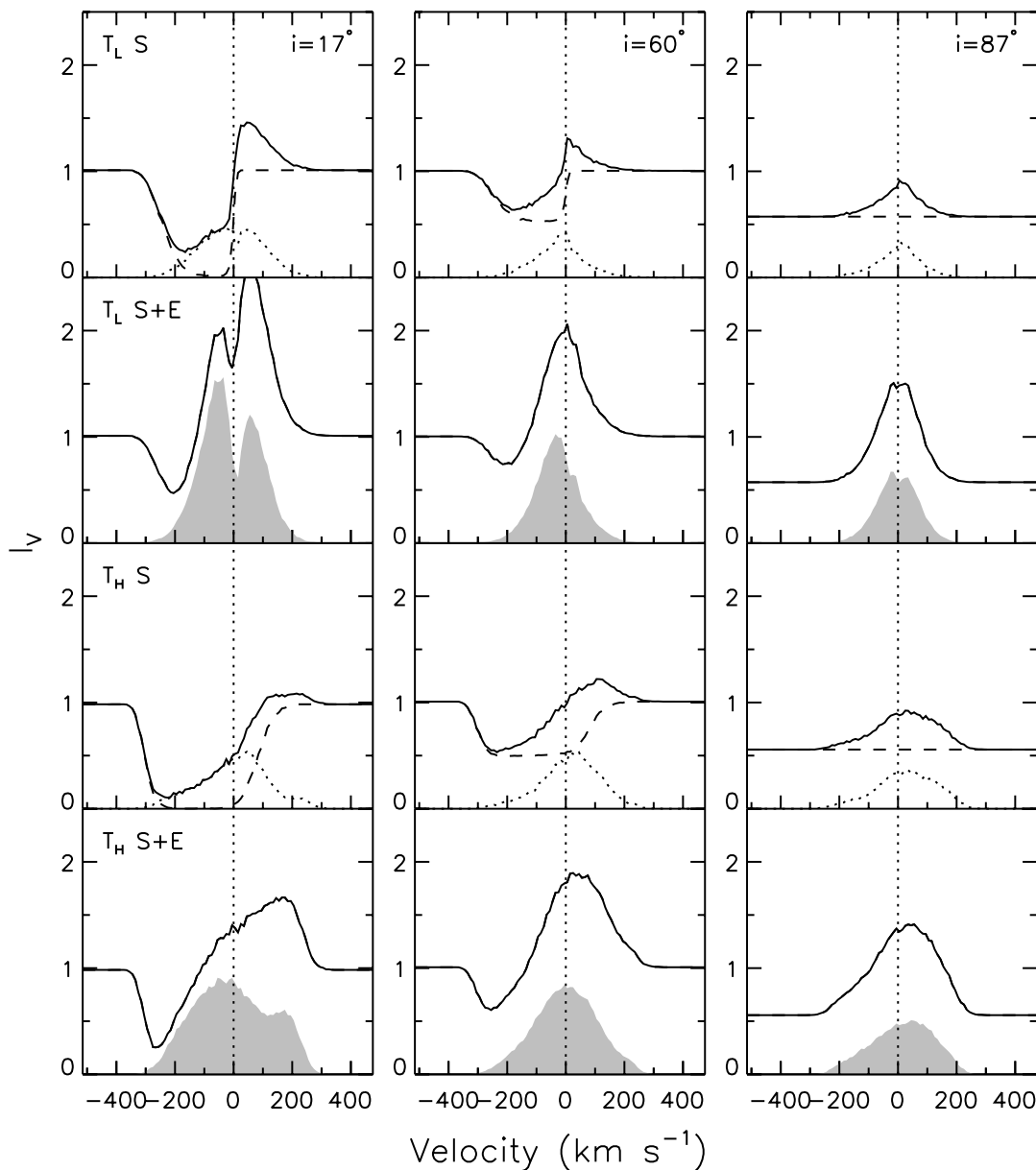


FIG. 6.—Polar stellar wind: profiles for a polar stellar wind emerging within 60° of the pole, for the same two cases of turbulence (T_L and T_H) with and without in situ emission (S and $S + E$) and including the effects of disk shadowing ($\rho r \leq r_i$), where $r_i = \rho r = 3.0R_*$. As before, vertical columns denote three viewing angles, $i = 17^\circ$, 60° , and 87° , measured from the disk normal.

observed level of this veiling continuum is much more strongly dependent on viewing angle. When this level is normalized to the observed stellar continuum level, the noticeable difference lies mostly in the part of the emergent spectrum above the continuum. This difference is not large and, since neither θ_w nor i is known in practice, it is reasonable to take scattering of the stellar continuum alone as representative, even when the veiling continuum is substantial.

In sum, the profile characteristics for stellar winds in the presence of disk shadowing are considerably more varied than those from disk winds. Both stellar and disk wind profiles are compared to the observed ones in § 3.

3. COMPARISON OF MODEL AND OBSERVED PROFILES

Our profile simulations for a range of disk and stellar wind configurations were motivated by the recent survey of He I $\lambda 10830$ in 38 CTTs (EFHK). They take advantage of the significant con-

tribution from scattering in this feature, unlike previous spectral diagnostics of inner winds in accreting systems. The comparisons necessarily focus on profile morphology, not intensity, which would require knowledge of the excitation conditions in the helium wind. This approach is helpful in determining whether the dominant signature of the inner winds in accreting T Tauri stars points to winds arising from the star or from the disk.

We highlight only general characteristics when comparing the data to our schematic model profiles in the absence of other relevant factors, particularly the relative contribution between scattering of continuum photons and in situ emission. Among the ensemble of disk wind models, there is a strong dependence of the line profile on viewing angle, ranging from a pure emission profile at $i < \theta_w$ to a line with a prominent absorption for $i > \theta_w$. The absorption feature is blueshifted with a fairly sharp redward edge, always narrow in comparison with the full range of wind velocities, and with a centroid becoming less blueshifted as i increases.

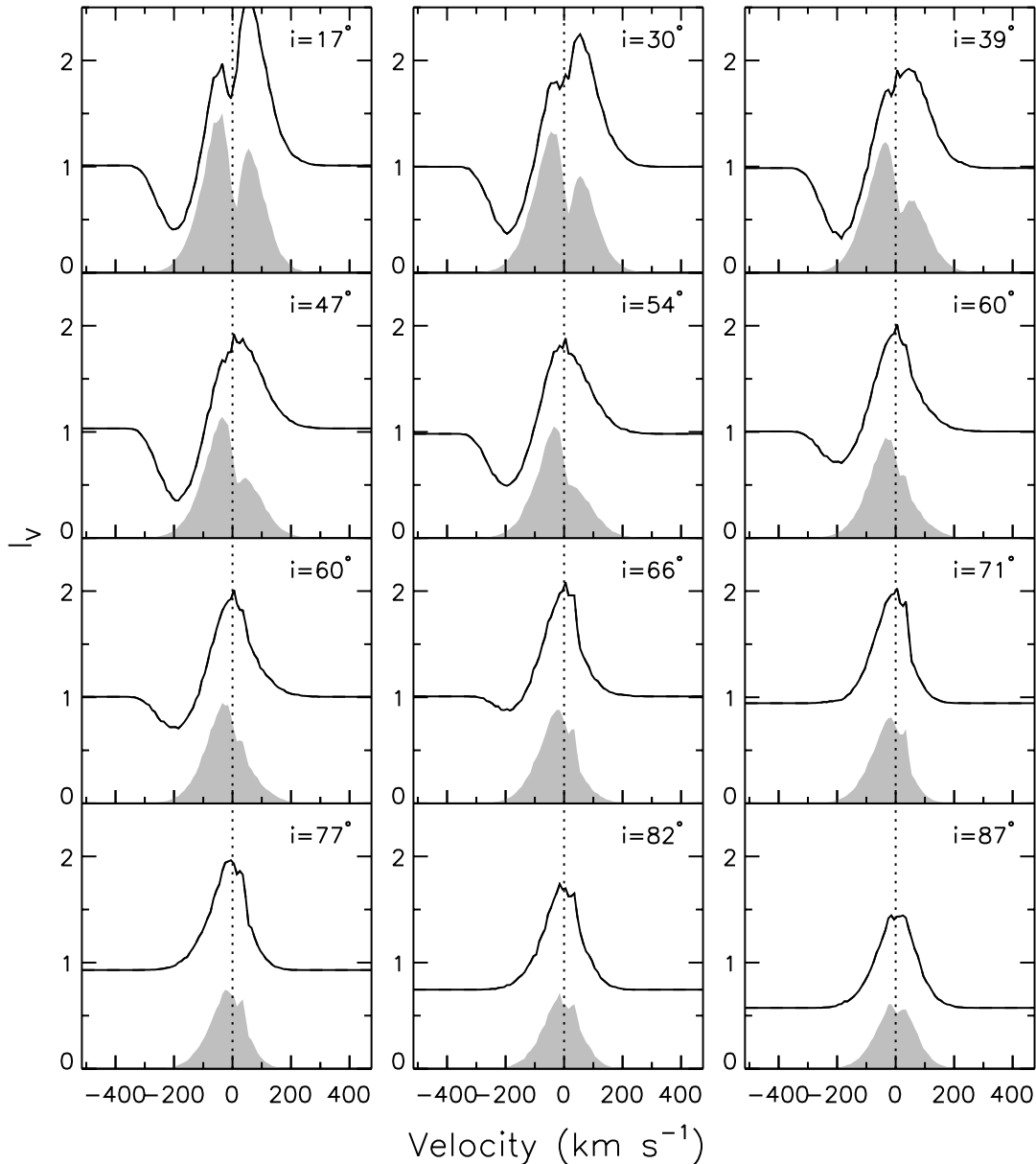


FIG. 7.—Polar stellar wind: profiles for the same polar wind with disk shadowing as Fig. 6, emerging within 60° of the pole with $r_i = \rho r = 3.0R_*$, except that all profiles are for low turbulence (T_L), all include in situ emission (E is the shaded area), and a much finer grid of viewing angles is shown, stepping from $i = 17^\circ$ to 87° .

For pure scattering, the emission above the continuum is very weak and has a broad, flattened shape from the combined rotational and poloidal motions. The aspect dependence of the emission morphology is more clearly delineated when in situ emission is included, transitioning from mostly blueshifted in pole-on views to a more centered profile with a central depression and double-horned structure in more edge-on views.

The stellar wind models show a greater variety of profile morphologies, arising from the effects of disk occultation, turbulence, and wind opening angle, along with the possibility of an in situ emission contribution to the pure scattering profile. Key predictions from the ensemble of stellar wind models are (1) a broad range, from highly negative to highly positive values, of the *net* equivalent width; (2) blue absorptions at all inclinations for spherical winds, but only for lines of sight inside or close to the wind opening angle for polar winds; (3) for the part of the profile below the continuum, absorption can occur over a broad range of possible depths and widths; (4) for the part of the profile above

the continuum, emission is single peaked, with centroids that can range from blueward to redward of the stellar velocity. Another characteristic of a stellar wind is that the blue absorption always reaches to the blueward edge of the profile, as it is very difficult to produce emission blueward of the absorption, even in the presence of strong in situ emission. This is because the in situ emission profile declines with increasing blueward velocity faster than the corresponding shallowing of the absorption profile, which is likely to be troughlike once the line opacity exceeds unity.

3.1. Assessment of Disk and Stellar Wind Candidates from Profiles with Blue Absorption

Our initial comparison of model and observed profiles focuses on those He I $\lambda 10830$ profiles with blue absorption features, a clear signature of an inner wind. Figures 9 and 10 show the 26/38 He I $\lambda 10830$ profiles from EFHK with blue absorptions strong enough to compare to our wind models, where the former are identified as having blue absorptions resembling disk winds and the latter

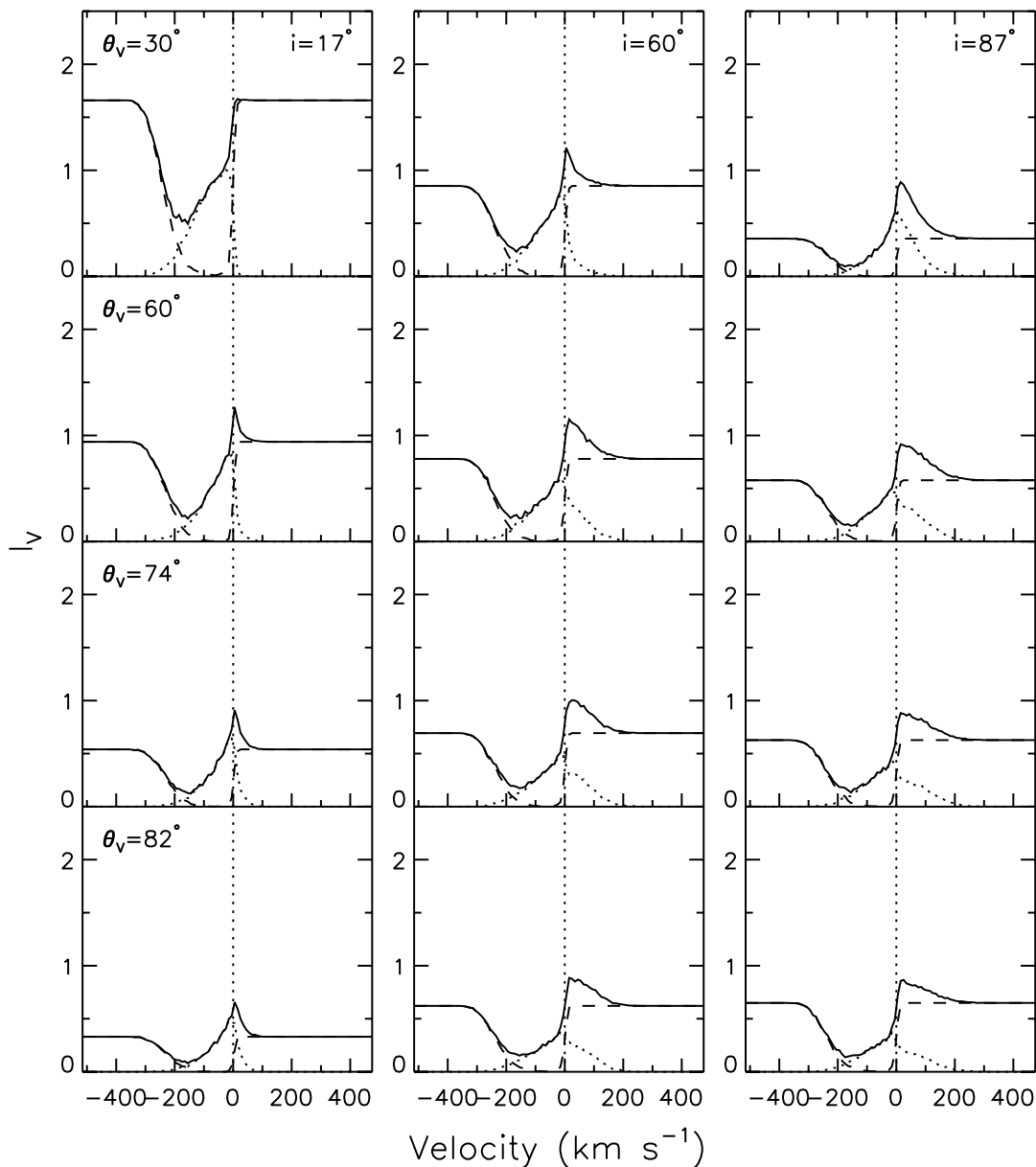


FIG. 8.— Stellar wind: pure scattering profiles of a stellar wind with the incident photons arising from a continuum source restricted to an axisymmetric ring at a polar angle θ_v on the star with width $\Delta \cos \theta = 0.1$. All cases are for low turbulence, T_L , and $\rho_T = 1R_*$. The four rows represent four rings with $\theta_v = 30^\circ, 60^\circ, 74^\circ$, and 82° . Vertical columns denote viewing angles $i = 17^\circ, 60^\circ$, and 87° , measured from the disk normal. The vertical scale illustrates how the observed veiling continuum level depends on θ_v and i . Its actual value relative to the stellar continuum (set to 1 at $i = 0^\circ$) is obtained by multiplying the plotted value by the factor $0.1(e^{1.33/T_v} - 1)/(e^{1.33/T_*} - 1)$, where T_* and T_v are the stellar and veiling continuum temperature, in units of 10^4 K, respectively.

as having stellar winds. Some of the observed profiles have a close resemblance to model profiles (e.g., DK Tau and CI Tau for disk winds and HL Tau and DF Tau for stellar winds), making the categorization straightforward. Others are less clear (e.g., DL Tau and DQ Tau), and for these we use both (1) the presence of emission blueward of the blue absorption and (2) the shape of the transition between the blue absorption and the emission to its redward edge to guide our selection in ambiguous cases, as described below.

Figure 9 assembles helium profiles from 11 CTTSs from the EFHK survey with blueshifted absorption that we identify as disk wind candidates: DK Tau, CI Tau, SU Aur, DS Tau, UZ Tau E, RW Aur B, AA Tau, V836 Tau, DL Tau, UY Aur, and GG Tau (sorted by profile morphology). The majority (9) also show redshifted absorption that presumably arises in a magnetospheric funnel flow, but these appear to be separately formed, as it does not appear that either the blue or red absorption is filled in by the scat-

tered photons from the other flow. Directing attention to the blue sides of the line profiles, there are three stars with profiles closely resembling those of the disk wind models with no in situ emission and $i > \theta_w$, i.e., narrow subcontinuum blue absorption and little or no emission. These are DK Tau, CI Tau, and SU Aur, shown in the top row of Figure 9. The other eight stars with blueshifted absorption resembling predictions for a disk wind also have helium emission, but this emission does not have the character expected from a disk wind, which would be broad and flattened and possess rotational peaks for viewing angles large enough to witness blue absorption ($i > \theta_w$). These 11 profiles thus suggest that the disk wind is not an important source of helium emission, which must arise from another source. In a couple of objects (V836 Tau and DL Tau) the depth of the absorption indicates that not only the continuum, but also a part of the line emission, is absorbed, suggesting that the source of emission is interior to the absorbing disk wind. In

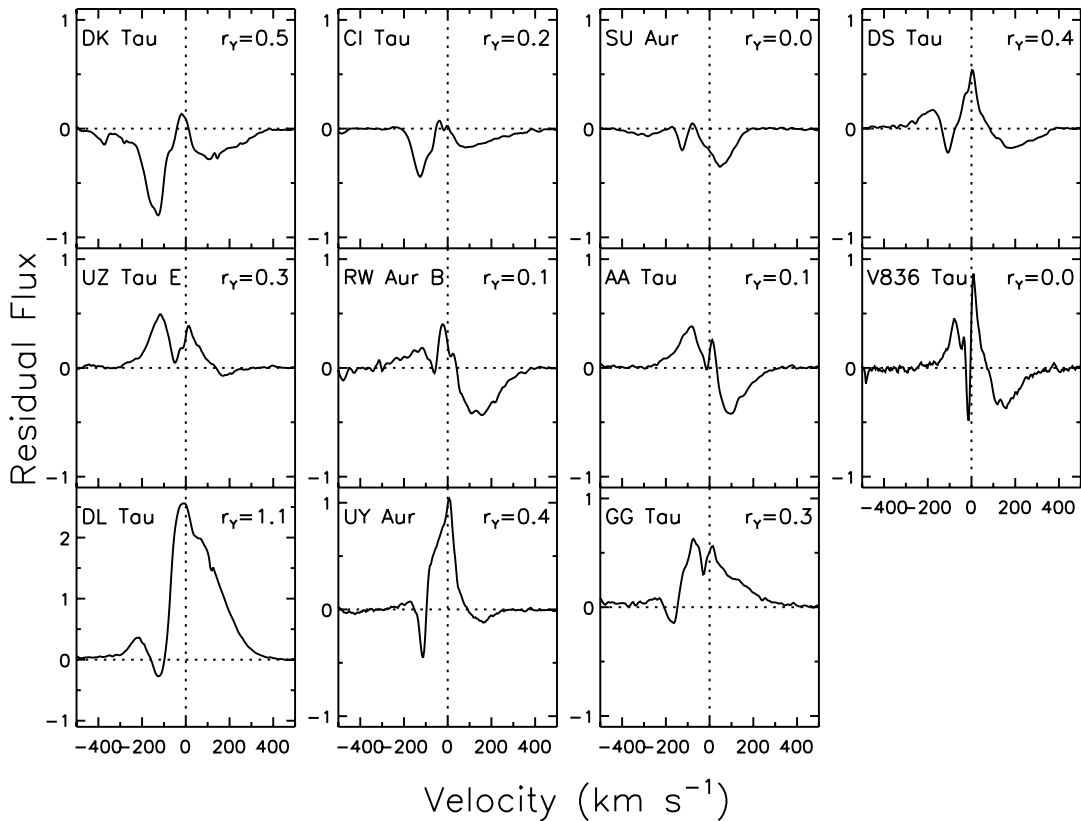


FIG. 9.—Observed profiles of He I $\lambda 10830$ for 11 CTTSs (from EFHK) with blueshifted absorption resembling the disk wind models. Sorting is by profile morphology.

§ 3.2 we argue that the helium emission likely arises via in situ emission in a stellar wind, and the narrow, blue absorptions that we ascribe to the disk wind cut into this stellar wind emission. For several stars the blue absorptions cutting into the emission are narrower than those in our disk wind model profiles (e.g., V836 Tau and UY Aur), but this could result by simply narrowing the range between ρ_i and ρ_f for the helium disk wind.

Common to all the profiles in the disk wind category is that, when helium emission is present, it extends blueward of the narrow, shallow blue absorption feature. In stellar wind models, which can also produce narrow and shallow blue absorption when in situ emission is strong, the blue absorption always reaches to the blueward edge of the profile. In contrast, for a disk wind the narrow absorption may be located anywhere blueward of line center; however, it is not likely to be strong near the wind terminal velocity. This is because, although the wind poloidal velocity has a large line-of-sight component for viewing angles near the wind opening angle, θ_w , the sight lines toward the stellar surface intersect the disk wind at large distances from the disk plane, where the gas density and excitation conditions are less likely to favor a high opacity in the He I $\lambda 10830$ transition. Thus, if there is obvious emission extending blueward of the blue absorption, we categorize the absorption as arising in a disk wind, with the emission arising from a second source.

A second criterion guiding our selection of blue absorption from disk versus stellar winds is the shape of the transition between the blue absorption and the emission to its redward edge, which is different in the two models. In a stellar wind with pure scattering, the blue absorption gives way smoothly to the red emission, like a slanted S written from left to right. Even with the addition of in situ emission, the emergent profile shows a smooth transition between the blue absorption and the emission component. In contrast, for the disk wind the pure scattering profile has

a distinct absorption feature with little emission on either side, and when an in situ emission profile is added, there is a two-component appearance, as if the absorption feature had a “bite” taken out of a separate emission feature.

With these additional criteria in mind, 15 stars from the EFHK He I $\lambda 10830$ survey, assembled in Figure 10, are identified as stellar wind candidates: DR Tau, AS 353A, HL Tau, GW Ori, TW Hya, DO Tau, DF Tau, CY Tau, DG Tau, XZ Tau, HK Tau, DE Tau, GI Tau, DN Tau, and DQ Tau (sorted by profile morphology). Only four of these also show subcontinuum red absorption from a funnel flow, which again we assume does not impact the blue absorption from the wind. The profiles among the stellar wind candidates are quite varied. Their net equivalent widths range from highly negative (DR Tau) to highly positive (DG Tau), and their emission centroids range from redshifted (AS 353A, GW Ori, and DF Tau) to blueshifted (HK Tau, XZ Tau, and DN Tau). In all cases the blue absorption extends to the blue edge of the profile, although it ranges from very broad and deep (DR Tau, AS 353A, HL Tau, and GW Ori) to rather narrow and shallow (DG Tau, HK Tau, GI Tau, and DN Tau).

In contrast to the disk wind candidates, in which disk winds account only for the absorption, but not the emission, component of the line, here the array of combined absorption and emission components is well reproduced by the stellar wind models, when the effects of disk shadowing, in situ emission, and turbulence are considered. Some profiles resemble those predicted from pure scattering, although they also require disk shadowing, where $\rho_T \leq r_i$, in order to create large negative equivalent widths (DR Tau) and/or turbulence in order to reproduce red emission peaks (DR Tau, AS 353A, and HL Tau). The contribution of in situ emission is required for stellar wind candidates with a net positive equivalent width (e.g., DG Tau and TW Hya), and a combination of in situ emission and disk shadowing is necessary to

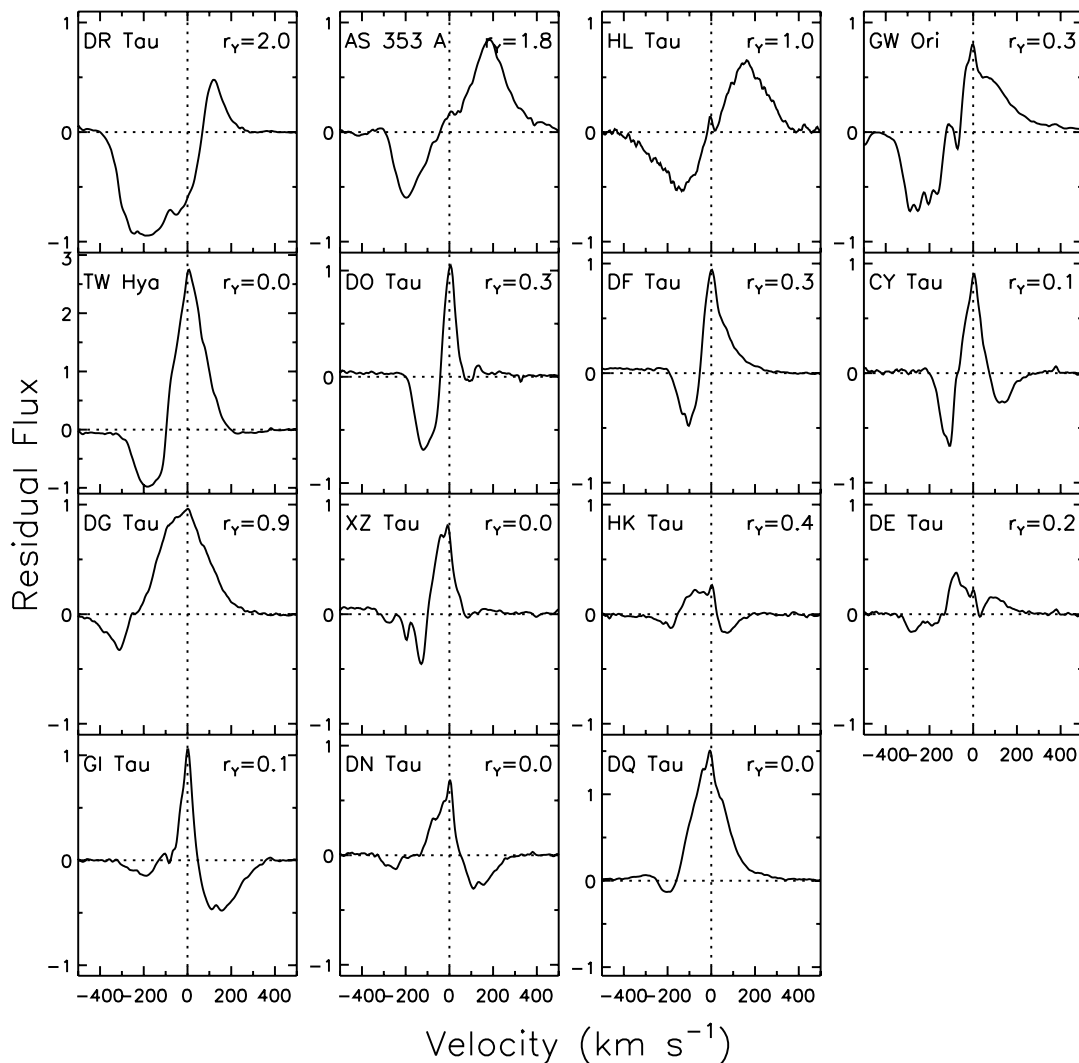


FIG. 10.—Observed profiles of He I $\lambda 10830$ for 15 CTTs (from EFHK) with both blueshifted absorption and emission features resembling the stellar wind models. Sorting is by profile morphology.

produce blue emission centroids (e.g., DG Tau, XZ Tau, HK Tau, and DN Tau).

We recognize that some of our categorizations are not clear-cut cases for disk or stellar winds, especially objects like DQ Tau, where the presence of emission blueward of the blue absorption may or may not be present, or GG Tau, where absorptions from both stellar and disk winds may be present. With this caveat, our comparison of blueshifted absorptions in observed He I $\lambda 10830$ profiles from EFHK with those predicted from disk and stellar wind models suggests a roughly comparable number of stars with disk wind and with stellar wind signatures. We anticipate that a more definitive assessment will be possible when simultaneous He I $\lambda 10830$ and He I $\lambda 5876$ profiles are available, as discussed in § 3.2. A summary of the profile assignments follows.

1. We find 11/38 CTTs (29%) with blue absorption at He I $\lambda 10830$ that resemble those expected for disk winds. Of these, eight also have helium emission, but with a morphology inconsistent with formation in a disk wind viewed at an angle exceeding the opening angle of the wind, as required for formation of their blue absorption (Fig. 9).

2. We find 15/38 CTTs (39%) with blue absorption at He I $\lambda 10830$ that have profiles consistent with formation in stellar winds (Fig. 10). Here both absorption and emission components

of the profiles can be accounted for by the stellar wind models when disk shadowing and in situ emission are included.

At least one other region besides disk and stellar winds is clearly contributing to the formation of He I $\lambda 10830$ —the (presumably) magnetospheric accretion columns channeling infalling material from the inner disk to the star, signified by redshifted absorption. Redshifted subcontinuum absorption is seen in 47% (18/38) of the CTTs in the EFHK survey, distributed such that 9 are seen among the 11 stars with disk wind profiles, but only 4 among the 15 stars with stellar wind profiles. The additional 12/38 (31%) CTTs from EFHK that lack blue absorptions are shown in Figure 11. Their characteristics are identified below.

1. In four stars (CW Tau, HN Tau, RW Aur A, and BP Tau), helium is entirely in emission, with a blue centroid, but no subcontinuum absorption.

2. Four stars (FP Tau, GK Tau, UX Tau, and YY Ori) have little helium emission, but subcontinuum absorption that is at rest relative to the star, in two cases penetrating up to 50% of the continuum. Two also have redshifted subcontinuum absorption.

3. Two stars (BM And and LkCa 8) have simple reverse P Cygni profiles (and thus redshifted subcontinuum absorption).

4. Two stars (DD Tau and UZ Tau W) have helium too weak to render an analysis.

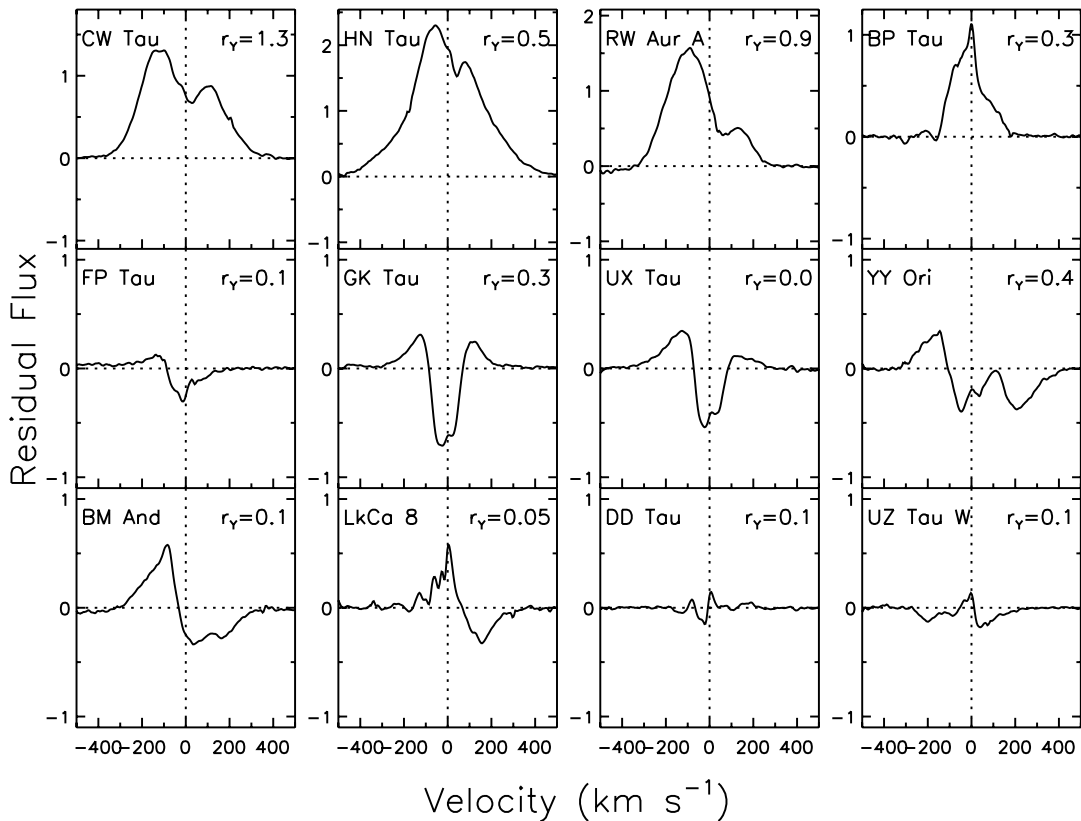


FIG. 11.—Observed profiles of He I $\lambda 10830$ for 12 CTTSs (from EFHK) lacking defining subcontinuum blueshifted absorption to permit classification as disk or stellar winds. Sorting is by profile morphology.

While neither disk winds, stellar winds, nor funnel flows are good candidates for the mysterious deep central absorption feature seen in four stars in Figure 11, we consider it likely that the remaining features in the helium lines in the EFHK survey can be accounted for by a combination of one or more of these three phenomena. In § 3.2 we further explore the He I $\lambda 10830$ profiles for clues to the presence of disk winds, stellar winds, or magnetospheres.

3.2. In Situ Emission and Blue Centroids

In § 3.1 we compared observed He I $\lambda 10830$ profiles to those predicted from disk or stellar wind models and concluded that disk wind signatures, when present, were signified only by the properties of the blue absorption, not by the emission component of the helium profile. In contrast, for profiles attributed to stellar winds, both their blueshifted absorption and their emission above the continuum could be accounted for with varying degrees of disk shadowing, in situ emission, and turbulence. We examine in this section the possibility that the helium emission in most CTTSs arises in a stellar wind, whether or not the profile also shows blue absorption from this wind. The “emission component” of $\lambda 10830$ will be a combination of scattering plus true emission arising in situ. The relative proportion between scattering and emission cannot be identified from profile morphology alone except in extreme cases. If the net equivalent width is zero or negative, it implies that scattering is dominant, with some occultation from disk or star, or if it is very positive, a significant amount of in situ emission must be present along with the scattering.

Of particular interest are the four stars in Figure 11 showing He I $\lambda 10830$ solely in emission, with no blue- or redshifted subcontinuum absorption. For these, the helium emission is single peaked, has a blueshifted centroid, and, in three of them, also

extends blueward in excess of 300 km s^{-1} . Single-peaked emission with blueshifted centroids can arise in stellar winds with occultation from the disk/star (see Figs. 4 and 6) or in magnetospheric funnel flows. In the case of the funnel flows, such profiles will result if the line in question has similar excitation conditions along the full arc of the magnetic accretion column, so the full range of infall velocities can contribute to the profile (Muzerolle et al. 2001; BEK).

In the case of stellar winds, one possibility for producing a pure emission profile is for the in situ emission to be so strong that it overwhelms the scattering contribution, so no subcontinuum absorption will be seen. This does not appear to be the case for He I $\lambda 10830$, however, since the observed peak flux density exceeds the continuum flux density by an amount that is only comparable to the latter. In the spherical stellar wind model profiles with in situ emission (second rows of Figs. 3 and 4), even if the in situ emission contribution is doubled beyond what is shown, the emergent profile will still show a blue absorption, albeit shallower and more displaced to the blue, while the peak flux density will be enhanced up to 3.5 times the continuum value. This difficulty in producing a pure emission profile via strong in situ emission arises because the in situ emission profile declines with increasing blueward velocity faster than the corresponding shallowing of the absorption profile, which is likely to be troughlike once the line opacity exceeds unity.

A more likely means of generating He I $\lambda 10830$ entirely in emission in a stellar wind is one where the wind emerges from latitudes toward the pole and is absent at latitudes close to the equator. From our model profiles for a polar stellar wind in Figure 7, it can be seen that as the viewing angle increases from $i = 0^\circ$ to 90° , the combined profile of scattering plus in situ emission progresses from P Cygni–like to a profile with stronger

emission and a more displaced, weaker blue absorption, and then to a purely emission profile that is blueshifted in the presence of disk occultation, except for the most extreme edge-on views. Another scenario might be an absence of spherical symmetry in the gas properties and/or excitation conditions. Since the absorption of the stellar continuum arises from the column of gas directly in front of the stellar surface, while both the photons scattered into the line of sight and the in situ emission come from a much larger region, inhomogeneities or variations in the physical conditions will likely affect the absorption part more and may produce a weaker absorption, more critically at the higher velocities. Time monitoring of the He I $\lambda 10830$ profile can test this possibility.

Given that single-peaked helium emission with a blueshifted centroid could signify either stellar winds or magnetospheric funnel flows (with the caveats outlined above for each), in the following three points we argue in favor of a stellar wind for the origin of helium emission over that from a magnetospheric funnel flow.

1. Among the 15 stars in Figure 10 with blueshifted absorption resembling stellar winds, there is a continual progression of He I $\lambda 10830$ profiles from absorption dominant to emission dominant. As shown in § 3.1, a radially accelerating stellar wind readily produces the characteristics of the deep and broad blue absorption shown by these stars. In situ emission arising in the same wind, with varying degrees of contribution relative to the scattering profile (dependent on physical conditions), can explain the rest of the profile morphology. Invoking a second source for the helium emission, i.e., a funnel flow, thus seems unnecessarily complicated when the same wind producing the absorptions will suffice. Moreover, a funnel flow origin for the helium emission in these 15 stars would be difficult to reconcile with the observation that they are considerably less likely to have simultaneous subcontinuum red absorption from funnel flows than the rest of the sample (27% vs. 60%).

2. A wind origin most readily accounts for the broad component emission in a closely related line in the helium triplet series, He I $\lambda 5876$, which is the immediate precursor to He I $\lambda 10830$ in a recombination/cascade sequence. This line is one of the strongest emission lines at optical wavelengths after the Balmer and Ca II lines and has a kinematic structure composed of distinct broad- (BC) and narrow-component (NC) emission (BEK). The $\lambda 5876$ BC emission is optically thin and thus directly probes the in situ helium emission. Its kinematic properties usually suggest an origin in outflowing gas, with centroids either blueshifted in excess of 30 km s^{-1} or less blueshifted, but with blue wing velocities exceeding that expected from an accretion flow (in excess of -200 km s^{-1}). If the blue centroid BC emission did arise in the accretion flow, then one would expect a correlation between the He I $\lambda 5876$ NC formed in the accretion shock and the blue centroid BC. In fact, BEK show that the opposite is true. When the blue centroid BC is strong, the NC is absent or weak. In contrast, while the NC is strong, the BC is absent or weak and sometimes shows a redshift. A simple explanation for this is that when in situ helium emission arises from the funnel flow, it is weak, and its red centroid results from the fact that the excitation of $\lambda 5876$ emission comes primarily from the terminus of the funnel flow in close proximity to the hot accretion shock. Correspondingly, the more prominent and more frequent $\lambda 5876$ blue centroid BC arises from a stellar wind, which will be the same flow producing the He I $\lambda 10830$ profile. (The absence of NC emission from an accretion shock at He I $\lambda 10830$ is discussed in § 4.)

3. The He I $\lambda 10830$ and $\lambda 5876$ transitions have upper states that are more than 21 eV above the ground state. Either a temperature exceeding 20,000 K or a strong UV continuum flux is needed for excitation. These conditions, although seemingly challenging,

must be present, as the lower level of He I $\lambda 10830$ is excited in at least three different kinematic regions (namely, stellar wind, disk wind, and magnetospheric infall), through its unmistakable absorption features. While for a stellar wind only a small fraction of the energy required to accelerate the wind to 300 km s^{-1} or more need be tapped to heat or ionize the gas (perhaps through magnetic field reconnection), for a magnetospheric funnel flow no energy is needed for the infalling gas to free-fall to the star. Thus, there is a natural way for a wind to generate sufficient heating, but no reason to expect this from the funnel flow beyond the modest heating from adiabatic compression of the converging flow (Martin 1996). If the gas excitation in the magnetospheric funnel flow is caused instead by photoionization, either from the accretion shock at the terminus of the funnel flow or from the stellar corona, or both, it is reasonable to expect that the funnel flow near the terminus will be more strongly excited, because of proximity and possible attenuation of ionizing photons before reaching the beginning of the funnel flow. The resulting spatial dependence of the helium excitation would produce a redshifted BC from the funnel flow, rather than a blueshifted one (as sometimes seen by BEK in He I $\lambda 5876$).

Based on the above arguments attributing in situ He I $\lambda 10830$ emission with blue centroids to stellar winds, we conclude that in addition to the 15 objects with blueshifted absorptions resembling stellar winds, at least 9 more objects may also have a stellar wind contribution to $\lambda 10830$. These include the four stars in which helium is entirely in emission (CW Tau, HN Tau, RW Aur A, and BP Tau in Fig. 11) and another five stars with a blue absorption indicative of a disk wind, but emission resembling that expected from in situ emission in a stellar wind (DS Tau, UZ Tau E, DL Tau, UY Aur, and GG Tau in Fig. 9). What is shared by these nine stars with in situ helium emission, in varying degrees of intensity, is single peaked and somewhat blueshifted emission (assuming those with blue absorptions from disk winds can be reconstructed by interpolating over the narrow absorption). All but one also have blueward wing velocities exceeding 300 km s^{-1} , well in excess of model profiles produced in a funnel flow (Muzerolle et al. 2001). Adding these 9 to the previous 15 makes a total of 24/38 (63%) objects in the EFHK survey as good candidates for helium-emitting stellar winds.

This leaves 14 stars for which we find no persuasive evidence for a stellar wind contribution at helium. Among these, five have helium profiles with net helium equivalent widths near zero, as expected for profiles formed by pure scattering. In each of these five, a broad and deep redshifted absorption is offset by comparably strong blueshifted “emission,” so that the full reverse P Cygni-like profile could be explained by scattering in the funnel flow (BM And and LkCa 8 in Fig. 11 and RW Aur B, AA Tau, and V836 Tau in Fig. 9). The remaining nine stars have “emission” components too weak to be interpreted, either because the emission is intrinsically weak or there is a deep central absorption feature rendering the helium emission indecipherable.

We conclude that there is good consistency in the evidence for helium-emitting stellar winds in accreting T Tauri stars between the He I $\lambda 10830$ and He I $\lambda 5876$ lines, although, in the absence of simultaneous optical and near-infrared spectra, it is problematic to draw conclusions from individual stars. It is also clear that He I $\lambda 10830$, with its high frequency of subcontinuum blueshifted absorption, is the more definitive diagnostic of a stellar wind. However, while the He I $\lambda 10830$ line is an excellent probe of the kinematic behavior of gas in the vicinity of the star, by itself it is not a strong diagnostic of physical conditions, since to scatter stellar photons, it needs only a line opacity of greater than or about unity. For example, if helium excitation is via thermal collisions,

then for a temperature between 20,000 and 40,000 K, the mass-loss rate for a spherical stellar wind need only be greater than or about $10^{-9} M_{\odot} \text{ yr}^{-1}$ to reach an optical depth of unity (J. Kwan et al. 2007, in preparation). Good constraints on the physical conditions in these kinematic regions await simultaneous observations of He I λ 10830 and λ 5876.

4. DISCUSSION

4.1. Winds and Magnetospheric Accretion

The high opacity of He I λ 10830 provides extraordinary sensitivity to both winds (from the disk and star) and funnel flows via absorption of continuum photons. This allows for a comparison of the prominence of each of these phenomena in relation to each other. The He I λ 10830 profiles from the EFHK survey show a clear tendency for magnetospheric accretion signatures to be more prevalent in stars with blue absorption from disk winds (82% of the stars in Fig. 9) than those with blue absorption from stellar winds (27% of the stars in Fig. 10). A viable explanation for this could be an inclination effect, if both stellar and disk winds are simultaneously present, along with magnetic funnel flows, and the stellar winds emerge from polar latitudes. In that case polar viewing angles would favor the appearance of P Cygni profiles from the stellar wind, while equatorial viewing angles would favor the appearance of narrow blue absorption from disk winds, along with red absorption from funnel flows.

If the above scenario is correct, we would expect large viewing angles for stars with blue absorption from a disk wind. Constraints on inclination for stars with stellar wind signatures are less clear, since the opening angle of the wind will also be important in determining whether blue absorption is visible. A literature search turns up inclination estimates for 23 of the 38 CTTSs in the EFHK survey, estimated from a variety of techniques, including those based on (1) measurements of rotation period and $v \sin i$, coupled with an estimate of the stellar radius (Ardila et al. 2002; Appenzeller et al. 2005), (2) axial ratios of resolved disks (Close et al. 1998; Simon et al. 2000), and (3) measured and/or inferred radial velocities and proper motions of resolved microjets (Lavalley-Fouquet et al. 2000; López-Martín et al. 2003; Hartigan et al. 2004). Often inclinations are not well constrained; different techniques applied to the same star can yield estimates differing by 20° – 40° or more. With these large uncertainties, the value of matching profiles with published inclinations is unclear. However, the published inclinations do not indicate any serious contradictions to our basic scenario. Among the stars with blue absorptions attributed to disk winds, the seven published inclinations range from 40° to 80° , consistent with viewing at inclinations high enough for lines of sight through the disk wind. Dupree et al. (2005) looked at He I λ 10830 profiles in two CTTSs with low inclinations ($<20^{\circ}$), namely, TW Hya and T Tau, and found both had P Cygni profiles resembling stellar winds. The four stars with blueshifted helium emission and no blue absorptions that we attribute to viewing a polar stellar wind from inclinations exceeding the wind opening angle are RW Aur at $i = 46^{\circ}$, CW Tau at $i = 49^{\circ}$, HN Tau at $i = 60^{\circ}$ – 70° , and BP Tau at $i = 30^{\circ}$ – 40° (see above references). We hesitate to draw any firm conclusions from published inclinations, however, not only because many have large uncertainties, but also because misalignments between magnetic and rotation axes may be present.

Another effect may also contribute to the less frequent combination of stellar wind and magnetospheric accretion signatures. Of the seven stars in the EFHK survey with the highest $1 \mu\text{m}$ veilings (r_V on the order of unity or greater), all have helium pro-

files attributed to stellar winds (blue absorption and/or blue centroid emission), only one also has blue absorption resembling a disk wind, and none show redshifted subcontinuum absorption from a funnel flow (r_V is identified for each profile in Figs. 9, 10, and 11). Assuming that higher $1 \mu\text{m}$ veilings indicate higher disk accretion rates, the absence of redshifted absorption and higher frequency of stellar wind signatures with high veiling could arise if disks with high accretion rates had their truncation radii squeezed, resulting in smaller funnel flows (less apparent redshifted absorption), while allowing larger opening angles for stellar winds from polar latitudes. This is consistent with the finding that the morphology for many of the stellar wind profiles at He I λ 10830 (Fig. 10) seems to require shadowing from disks extending within the wind origination radius. A similar scenario was also suggested by BEK, based on the relation between He I λ 5876 profile components and veiling, where an anticorrelation between the strength of the BC emission from a stellar wind and the strength of the NC emission from the accretion shock suggested that in the presence of strong stellar winds, accretion shock formation is inhibited. This effect is also coupled with a different proportionality between the strength of the He I λ 5876 NC emission from the accretion shock and the amount of optical veiling, suggesting that optical veiling may not be dominated by the accretion shock in the presence of strong stellar winds. This could signify a transformation in the magnetic field geometry in stars of high veiling, allowing the disk to encroach well inside the corotation radius, reducing the size of the accreting funnel flow and setting up conditions for a wind to emerge radially from the star.

Unfortunately, the He I λ 10830 profiles do not provide the opportunity to trace the presence of an accretion shock from magnetospheric funnel flows through NC emission. This is, at first glance, surprising. In contrast to He I λ 5876 profiles, many of which show a prominent NC (BEK), this behavior is not conspicuous at λ 10830, although NC emission may be present in six objects (DS Tau, UY Aur, GI Tau, DN Tau, BP Tau, and LkCa 8), if the small emission spike near the stellar velocity is a distinct and separate feature from the rest of the profile. Thus, since the He I λ 10830 transition is more easily excited than the closely coupled He I λ 5876 transition, the paucity of NC emission at λ 10830 appears incongruous. We think two reasons account for this apparent discrepancy. First, the NC is formed in the postshock region of a magnetospheric funnel flow, where the very high gas density makes it likely that both transitions are optically thick and have nearly the same excitation temperature. With a high excitation temperature for both transitions, the He I λ 10830 intensity can be weaker than the He I λ 5876 intensity. When this is coupled to the fact that the stellar continuum is higher at $1.083 \mu\text{m}$ than at 5876 \AA , the resultant emission at He I λ 10830 from this region will appear much less prominent. As an example, for a stellar temperature of 3500 K and excitation temperatures of 15,000 and 20,000 K, the He I λ 10830 peak amplitude relative to its local continuum will be $1/8.7$ and $1/10$, respectively, of the He I λ 5876 peak amplitude relative to its local continuum. If the veiling at 5876 \AA , r_V , and that at 10830 \AA , r_Y , are significant, the above factor has to be multiplied by $(1 + r_Y)/(1 + r_V)$. Second, a stellar wind, when present, will scatter the NC. Occultation by the star and the disk will diminish its observed intensity, and turbulence in the initial acceleration of the wind will broaden its profile. This effect is much more important for the He I λ 10830 NC than for the λ 5876 NC, as the λ 5876 transition in the stellar wind region has a much smaller opacity. For these two reasons, it is understandable why the He I λ 10830 NC is absent in objects with strong wind signatures and much less conspicuous, in comparison with the λ 5876 NC, in objects with weak or no wind signatures.

4.2. Accretion-powered Disk and Stellar Winds

The ensemble of helium lines in CTTs suggests that both stellar and disk winds emerge from near stellar regions at velocities of several hundred km s^{-1} , where the prominence of one over the other at $\lambda 10830$ will depend in part on wind excitation conditions and viewing angle. The simultaneous presence of a disk and a stellar wind in an accreting young star is not surprising. Most theoretical treatments of disk winds assume, tacitly or explicitly, that a wind will also emerge from polar regions on the star. In most of these scenarios, stellar winds are assumed to be “ordinary” (Shu et al. 1994), i.e., scaled-up analogs of the solar wind, where hot coronal gas generates sufficient thermal pressure to accelerate material outward from the star. The observed X-ray fluxes from T Tauri stars clarify that “ordinary” coronal winds can at most generate mass-loss rates up to $10^{-9} M_{\odot} \text{ yr}^{-1}$ (deCampli 1981). Recent observations show that on average WTTs have X-ray fluxes several times higher than accreting CTTs (Feigelson et al. 2007), so any “ordinary” stellar wind would actually be stronger in a WTT than a CTT. The stellar (i.e., expanding radially away from the star) wind traced by He I $\lambda 10830$ is clearly not an “ordinary” one, since it is not detected in WTTs and it predominates in CTTs with the highest disk accretion rates. How such an accretion-powered, radially expanding wind is generated remains to be seen. Options for MHD-driven stellar winds summarized in Ferreira et al. (2006) include driving by turbulent Alfvén waves (Hartmann et al. 1982) and rotation (Hartmann & MacGregor 1980; Romanova et al. 2005), although CTTs are not rotating fast enough for the latter to be a major factor at this stage in their evolution. Conceivably, unsteady MHD phenomena that depend on the orientation of the magnetic moments of the stellar and disk fields, such as coronal mass ejections (e.g., Matt et al. 2002), could generate winds with the right geometry.

Disk winds have recently been put forward to explain $H\alpha$ profiles in CTTs (Kurosawa et al. 2006; Alencar et al. 2005). Although blue absorption with the characteristics of a stellar wind is rare at $H\alpha$, blue absorption consistent with disk winds is common. For example, CTT $H\alpha$ profiles from the BEK sample that closely overlaps the EFHK He I $\lambda 10830$ survey show only 10% with blue absorption penetrating the continuum, while 40% of the objects have sharp blue absorptions superposed on the broader line emission. In a more diverse sample of young stellar objects (Reipurth et al. 1996), more than 50% have such narrow, blue absorptions at $H\alpha$. As first suggested by Calvet (1997), this type of narrow, blue absorption at $H\alpha$ is likely formed in the disk wind. However, in a few CTTs, e.g., DR Tau and AS 353A (see profiles in BEK), $H\alpha$ has a distinct P Cygni character, with broad subcontinuum absorption on the blue edge of the emission profile, resembling profiles formed in stellar winds. In a larger number of stars, a stellar wind may be the source of at least some of the $H\alpha$ emission, as evidenced by the prevalence of blueward asymmetries in $H\alpha$ wing emission at velocities in excess of 200 km s^{-1} (BEK) and by resolved spatial extensions in the blue wings of $\text{Pa}\beta$ in some CTTs (Whelan et al. 2004). The rarity of $H\alpha$ or $H\beta$ profiles showing broad, blue subcontinuum absorptions from a stellar wind is not surprising, as the physical conditions for producing helium excitation (e.g., temperatures on the order of 20,000 K or higher for thermal collisions) will cause hydrogen to be mostly ionized. Thus, $H\alpha$ in the stellar wind would be more optically thin than He I $\lambda 10830$, but would still produce strong in situ emission via recombination/cascade.

An additional reason for suspecting that $H\alpha$ emission may arise partly in the stellar wind is the difficulty Kurosawa et al. (2006) had in reproducing both the emission and absorption con-

tributions to this line from a disk wind. Hybrid models that include both magnetospheric and disk wind contributions were used to calculate $H\alpha$ profiles with full radiative transfer and to self-consistently determine contributions from both infall and outflow regions for a specified ratio of disk accretion to mass outflow rates. However, in order to reproduce the observed range of $H\alpha$ profiles, including both emission and blue absorptions, disk wind opening angles in violation of the Blandford and Payne requirement for magnetocentrifugal launching had to be adopted. Furthermore, the tendency in CTTs for equivalent widths to increase with inclination (Appenzeller et al. 2005; White & Hillenbrand 2004) could not be explained. Instead, they found that an inclination-dependent equivalent width could be accounted for by replacing the disk wind with a bipolar wind emerging from the stellar polar regions. Within the context of the work presented here on He I $\lambda 10830$, these results could be reconciled if the stellar wind seen at helium is a major contributor to the $H\alpha$ emission, while the blue absorption at $H\alpha$ arises in a disk wind.

Warm disk wind models were also explored to account for CTTs semiforbidden lines in the ultraviolet, such as C III] and Si III], which are single peaked, broad, and blueshifted (Gomez de Castro & Ferro-Fontan 2005). The models required a very restricted set of assumptions to approximate the observed profiles. The profile morphology of the semiforbidden lines, however, is reminiscent of the helium emission seen in both He I $\lambda 10830$ and He I $\lambda 5876$, which we attribute to stellar winds.

The relative importance of disk and stellar winds in accreting systems is not yet clear. The new insight provided by He I $\lambda 10830$ and He I $\lambda 5876$ is that both are present in regions close to the star, both are “accretion powered,” and when disk accretion rates are high, a higher proportion of CTTs have helium profiles deriving from stellar winds. This suggests that the geometry of the star-disk interaction region is affected by the disk accretion rate, which likely has consequences for the evolution of angular momentum in the star.

5. CONCLUSIONS

The He I $\lambda 10830$ line in CTTs, through its propensity to absorb continuum radiation, provides a unique diagnostic of kinematic motions of the line formation regions close to the star. In this paper we have concentrated on the blue absorptions and, with the aid of theoretical models, have determined that both stellar and disk winds are traced by this line. While blue absorptions appear to arise in both disk and stellar winds, helium emission appears to arise only in the stellar wind or in a few stars with particularly deep red absorptions, possibly from scattering in magnetospheric funnel flows. Some of the stellar wind profiles also require significant disk shadowing to account for emission with blue centroids, indicating that the disk must extend interior to the radius where the wind is accelerated in these stars.

A larger fraction of the CTTs in the EFHK sample show stellar wind over disk wind signatures at He I $\lambda 10830$. However, in view of the more prevalent signature of disk wind absorptions at $H\alpha$, this probably indicates that excitation conditions for He I $\lambda 10830$ are more favorable in the stellar wind than in the disk wind. Both are likely present in most accreting stars, each contributing some, as yet unknown, fraction of the outflowing gas in the large-scale collimated outflows. The most likely scenario is that stellar winds emerge from the stellar polar regions above where magnetospheric funnel flows intercept the star. Not only does this allow both to coexist, but it also seems required to explain some stars that appear to have helium emission, but not helium absorption, from a stellar wind.

Evidence that stellar winds traced by helium are accretion powered comes from their absence in nonaccreting WTTSs and the fact that among stars with the highest disk accretion rates, including some Class I sources (EFHK), the stellar wind signatures are more frequent than disk wind signatures. This, coupled with the fact that the high accretion rate stars also rarely show redshifted absorption at He I λ 10830 from magnetospheric infall and have weaker NC emission at He I λ 5876 from magnetospheric accretion shocks, suggests the possibility that when disk accretion rates are high, magnetic accretion zones are smaller, and favorable conditions for stellar winds are enhanced. This may be an important aspect of the angular momentum regulation mechanism postulated by Matt & Pudritz (2005), where stellar winds act efficiently to carry away accreted angular momentum when accretion rates are high.

It is not yet clear what role an accretion-powered stellar wind plays in the formation of collimated jets or overall mass and angular momentum loss in accreting systems. While the He I λ 10830 line is an excellent probe of the kinematic behavior of gas in the vicinity of the star and thus speaks to the interaction of the stellar magnetosphere and the accretion disk, by itself it is not a strong diagnostic of physical conditions. Good constraints on the physical conditions in these kinematic regions await simultaneous ob-

servations of He I λ 10830 and λ 5876. The latter line is the immediate precursor to the former in a recombination/cascade sequence, so the excitation conditions of the two lines are intimately coupled, and they will make an ideal pair for evaluating the relative contribution between continuum scattering and in situ emission. This will constrain the physical conditions, including line opacities, electron densities, kinetic temperatures, and limits on the ionizing flux, which in turn will enable identification of the wind contribution to the profile and provide estimates of the wind mass-loss rate in the helium-emitting wind(s). The simultaneous data will also help decompose the λ 10830 line profile into separate contributions from scattering and in situ emission and may shed light on the wind opening angle and viewing angle. With this information, the relative importance of disk and stellar winds in accreting systems may be discernible.

Collaboration and regular conversations with Lynne Hillenbrand on related aspects of this project have contributed to the results of this paper. NASA grant NAG5-12996 issued through the Office of Space Science provides support for this project. We thank an anonymous referee for helpful comments that improved the presentation of this manuscript.

REFERENCES

- Alencar, S. H. P., Basri, G., Hartmann, L., & Calvet, N. 2005, *A&A*, 440, 595
 Appenzeller, I., Bertout, C., & Stahl, O. 2005, *A&A*, 434, 1005
 Appenzeller, I., & Mundt, R. 1989, *A&A Rev.*, 1, 291
 Ardila, D., Basri, G., Walter, F., Valenti, J., & Johns-Krull, C. 2002, *ApJ*, 566, 1100
 Bally, J., Reipurth, B., & Davis, C. J. 2007, in *Protostars and Planets V*, ed. B. Reipurth, D. Jewitt, & K. Keil (Tucson: Univ. Arizona Press), 215
 Beristain, G., Edwards, S., & Kwan, J. 2001, *ApJ*, 551, 1037 (BEK)
 Blandford, R. D., & Payne, D. G. 1982, *MNRAS*, 199, 883
 Calvet, N. 1997, in *IAU Symp. 182, Herbig-Haro Flows and the Birth of Stars*, ed. B. Reipurth & C. Bertout (Dordrecht: Kluwer), 417
 Carr, J. S., Tokunaga, A. T., & Najita, J. 2004, *ApJ*, 603, 213
 Close, L. M., et al. 1998, *ApJ*, 499, 883
 deCampli, W. M. 1981, *ApJ*, 244, 124
 Dougados, C., Cabrit, S., Lavalley, C., & Ménard, F. 2000, *A&A*, 357, L61
 Dupree, A. K., Brickhouse, N. S., Smith, G. H., & Strader, J. 2005, *ApJ*, 625, L131
 Edwards, S., Fischer, W., Hillenbrand, L., & Kwan, J. 2006, *ApJ*, 646, 319 (EFHK)
 Edwards, S., Fischer, W., Kwan, J., Hillenbrand, L., & Dupree, A. K. 2003, *ApJ*, 599, L41
 Edwards, S., Hartigan, P., Ghandour, L., & Andrulis, C. 1994, *AJ*, 108, 1056
 Feigelson, E., Townsely, L., Gude, M., & Stassun, K. 2007, in *Protostars and Planets V*, ed. B. Reipurth, D. Jewitt, & K. Keil (Tucson: Univ. Arizona Press), 313
 Ferreira, J., Dougados, C., & Cabrit, S. 2006, *A&A*, 453, 785
 Gomez de Castro, A., & Ferro-Fontan, C. 2005, *MNRAS*, 362, 569
 Hartigan, P., Edwards, S., & Ghandour, L. 1995, *ApJ*, 452, 736
 Hartigan, P., Edwards, S., & Pierson, R. 2004, *ApJ*, 609, 261
 Hartmann, L., Calvet, N., Avrett, E., & Loeser, R. 1990, *ApJ*, 349, 168
 Hartmann, L., Edwards, S., & Avrett, E. 1982, *ApJ*, 261, 279
 Hartmann, L., Hewett, R., & Calvet, N. 1994, *ApJ*, 426, 669
 Hartmann, L., & MacGregor, K. B. 1980, *ApJ*, 242, 260
 Hartmann, L., & Stauffer, J. 1989, *AJ*, 97, 873
 Königl, A., & Pudritz, R. E. 2000, in *Protostars and Planets IV*, ed. V. Mannings, A. P. Boss, & S. S. Russell (Tucson: Univ. Arizona Press), 759
 Kurosawa, R., Harries, T. J., & Symington, N. H. 2006, *MNRAS*, 370, 580
 Lavalley-Fouquet, C., Cabrit, S., & Dougados, C. 2000, *A&A*, 356, L41
 López-Martín, L., Cabrit, S., & Dougados, C. 2003, *A&A*, 405, L1
 Martin, S. C. 1996, *ApJ*, 470, 537
 Matt, S., Goodson, A. P., Winglee, R. M., & Bohm, K. H. 2002, *ApJ*, 574, 232
 Matt, S., & Pudritz, R. E. 2005, *ApJ*, 632, L135
 Muzerolle, J., Calvet, N., & Hartmann, L. 2001, *ApJ*, 550, 944
 Najita, J., Carr, J. S., & Mathieu, R. D. 2003, *ApJ*, 589, 931
 Najita, J. R., Edwards, S., Basri, G., & Carr, J. 2000, in *Protostars and Planets IV*, ed. V. Mannings, A. Boss, & S. S. Russell (Tucson: Univ. Arizona Press), 457
 Pudritz, R., Ouyed, R., Fendt, C., & Brandenburg, A. 2007, in *Protostars and Planets V*, ed. B. Reipurth, D. Jewitt, & K. Keil (Tucson: Univ. Arizona Press), 277
 Reipurth, B., Pedrosa, A., & Lago, M. T. V. T. 1996, *A&AS*, 120, 229
 Richer, J. S., Shepherd, D. S., Cabrit, S., Bachiller, R., & Churchwell, E. 2000, *Protostars and Planets IV*, ed. V. Mannings, A. P. Boss, & S. S. Russell (Tucson: Univ. Arizona Press), 867
 Romanova, M. M., Ustyugova, G. V., Koldoba, A. V., & Lovelace, R. V. E. 2005, *ApJ*, 635, L165
 Shu, F., Najita, J., Ostriker, E., Wilkin, F., Ruden, S., & Lizano, S. 1994, *ApJ*, 429, 781
 Simon, M., Dutrey, A., & Guilloteau, S. 2000, *ApJ*, 545, 1034
 von Rekowski, B., & Brandenburg, A. 2006, *Astron. Nachr.*, 327, 53
 Whelan, E. T., Ray, T. P., & Davis, C. J. 2004, *A&A*, 417, 247
 White, R. J., & Hillenbrand, L. A. 2004, *ApJ*, 616, 998